



# SILVERRUSH. VII. Subaru/HSC Identifications of Protocluster Candidates at $z \sim 6-7$ : Implications for Cosmic Reionization

Ryo Higuchi<sup>1,2</sup>, Masami Ouchi<sup>1,3</sup>, Yoshiaki Ono<sup>1</sup>, Takatoshi Shibuya<sup>1</sup>, Jun Toshikawa<sup>1</sup>, Yuichi Harikane<sup>1,2</sup>, Takashi Kojima<sup>1,2</sup>, Yi-Kuan Chiang<sup>4</sup>, Eiichi Egami<sup>5</sup>, Nobunari Kashikawa<sup>6,7</sup>, Roderik Overzier<sup>8</sup>, Akira Konno<sup>1,9</sup>, Akio K. Inoue<sup>10</sup>, Kenji Hasegawa<sup>11</sup>, Seiji Fujimoto<sup>1,9</sup>, Tomotsugu Goto<sup>12</sup>, Shogo Ishikawa<sup>13,14</sup>, Kei Ito<sup>7</sup>, Yutaka Komiyama<sup>6,7</sup>, and Masayuki Tanaka<sup>6</sup>

<sup>1</sup> Institute for Cosmic Ray Research, The University of Tokyo, 5-1-5 Kashiwanoha, Kashiwa, Chiba 277-8582, Japan; [rhiguchi@icrr.u-tokyo.ac.jp](mailto:rhiguchi@icrr.u-tokyo.ac.jp)

<sup>2</sup> Department of Physics, Graduate School of Science, The University of Tokyo, 7-3-1 Hongo, Bunkyo-ku, Tokyo 113-0033, Japan

<sup>3</sup> Kavli Institute for the Physics and Mathematics of the Universe (Kavli IPMU, WPI), The University of Tokyo, 5-1-5 Kashiwanoha, Kashiwa, Chiba 277-8583, Japan

<sup>4</sup> Department of Physics & Astronomy, Johns Hopkins University, 3400 N. Charles Street, Baltimore, MD 21218, USA

<sup>5</sup> Steward Observatory, University of Arizona, 933 North Cherry Avenue, Tucson, AZ 85721, USA

<sup>6</sup> Optical and Infrared Astronomy Division, National Astronomical Observatory, Mitaka, Tokyo 181-8588, Japan

<sup>7</sup> Department of Astronomical Science, Graduate University for Advanced Studies (SOKENDAI), Mitaka, Tokyo 181-8588, Japan

<sup>8</sup> Observatório Nacional, Rua José Cristino, 77. CEP 20921-400, São Cristóvão, Rio de Janeiro-RJ, Brazil

<sup>9</sup> Department of Astronomy, Graduate School of Science, The University of Tokyo, 7-3-1 Hongo, Bunkyo-ku, Tokyo 113-0033, Japan

<sup>10</sup> Department of Environmental Science and Technology, Faculty of Design Technology, Osaka Sangyo University, 3-1-1, Nakagaito, Daito 574-8530 Osaka, Japan

<sup>11</sup> Department of Physics and Astrophysics, Nagoya University Furo-cho, Chikusa-ku, Nagoya, Aichi 464-8602, Japan

<sup>12</sup> Institute of Astronomy, National Tsing Hua University, No. 101, Section 2, Kuang-Fu Road, Hsinchu, Taiwan

<sup>13</sup> Center for Computational Astrophysics, National Astronomical Observatory of Japan, Mitaka, Tokyo 181-8588, Japan

<sup>14</sup> Department of Science, Faculty of Science and Engineering, Kindai University, Higashi-Osaka, Osaka 577-8502, Japan

Received 2017 December 30; revised 2019 March 22; accepted 2019 April 5; published 2019 July 1

## Abstract

We report 14 and 26 protocluster candidates at  $z = 5.7$  and  $6.6$  over 14 and 16  $\text{deg}^2$  areas, respectively, selected from 2230 (259)  $\text{Ly}\alpha$  emitters (LAEs) photometrically (spectroscopically) identified using Subaru/Hyper Suprime-Cam (HSC) deep images (Keck, Subaru, and Magellan spectra, and literature data). Six out of the 40 protocluster candidates include one to 13 spectroscopically confirmed LAEs. We conduct Monte Carlo simulations to estimate how many protocluster candidates are found by chance for randomly distributed sources, and find that the effective number of protocluster candidates at  $z = 5.7$  (6.6) is six (five). By comparing with the cosmological  $\text{Ly}\alpha$  radiative transfer (RT) model reproducing the LAEs with reionization effects, we find that more than half of these protocluster candidates are progenitors of present-day clusters with mass of  $\gtrsim 10^{14} M_{\odot}$ . We then investigate the correlation between the LAE overdensity  $\delta$  and the  $\text{Ly}\alpha$  rest-frame equivalent width  $\text{EW}_{\text{Ly}\alpha}^{\text{rest}}$ , because the cosmological  $\text{Ly}\alpha$  RT model suggests that the slope of the  $\text{EW}_{\text{Ly}\alpha}^{\text{rest}}-\delta$  relation steepens toward the epoch of cosmic reionization (EoR), due to the existence of ionized bubbles around galaxy overdensities easing the escape of  $\text{Ly}\alpha$  emission from the partly neutral intergalactic medium. The available HSC data suggest that the slope of the  $\text{EW}_{\text{Ly}\alpha}^{\text{rest}}-\delta$  correlation does not evolve from the post-reionization epoch,  $z = 5.7$ , to the EoR,  $z = 6.6$ , beyond the moderately large statistical errors. There is a possibility that we could detect the evolution of the  $\text{EW}_{\text{Ly}\alpha}^{\text{rest}}-\delta$  relation from  $z = 5.7$  to 7.3 using the upcoming HSC observations that will provide large samples of LAEs at  $z = 6.6-7.3$ .

*Key words:* galaxies: evolution – galaxies: formation – galaxies: high-redshift

## 1. Introduction

Studying the physical process of cosmic reionization is one of the important subjects in astronomy today. Studies of the Gunn–Peterson effect and the  $\text{Ly}\alpha$  damping wing found in the continua of high-redshift quasi-stellar objects and gamma-ray bursts have suggested that cosmic reionization was completed by  $z \sim 6$  (Fan et al. 2006; Bolton et al. 2011; Goto et al. 2011; Chornock et al. 2013; McGreer et al. 2015), although some recent results show that the reionization process is patchy, based on the  $\text{Ly}\alpha$  opacity along the quasar sight lines (e.g., Becker et al. 2015; Bosman et al. 2018) in addition to exciting new results from the puzzling COLA1 galaxy (Hu et al. 2016; Matthee et al. 2018). Similarly,  $\text{Ly}\alpha$  emission in high-redshift galaxies has been used to investigate the ionization state of the intergalactic medium (IGM), because the  $\text{Ly}\alpha$  damping wing of H I gas in the IGM attenuates  $\text{Ly}\alpha$  photons from  $\text{Ly}\alpha$  emitters (LAEs). Recently, Konno et al. (2018) and Ouchi et al. (2018) constrained the neutral hydrogen fraction of the IGM to be  $x_{\text{HI}} \simeq 0.3 \pm 0.2$  at  $z = 6.6$  from the evolution of the  $\text{Ly}\alpha$

luminosity functions (LFs) and the angular correlation function based on the large samples of LAEs at  $z \sim 6-7$  (see also Malhotra & Rhoads 2004; Kashikawa et al. 2006; Ouchi et al. 2008, 2010; Ota et al. 2010; Konno et al. 2014).

Despite the fact that the mean values of  $x_{\text{HI}}$  at  $z \sim 6-7$  are constrained, it is still unclear what the ionizing photon sources of cosmic reionization are. Although there are several candidates for the major sources of cosmic reionization, many observations suggest that it is likely that star-forming galaxies are the major sources of cosmic reionization (Bouwens et al. 2015; Robertson et al. 2015; Ishigaki et al. 2017). In this case, theoretical models predict that star-forming galaxies emitting ionizing photons from young massive stars would ionize the IGM around galaxies; the ionized regions in the IGM are called ionized bubbles. Large ionized bubbles are expected to form in galaxy overdensity regions, where many star-forming galaxies exist in a small volume of the universe (Furlanetto et al. 2006; Ono et al. 2012; Matthee et al. 2015; Ishigaki et al. 2016; Overzier 2016; Chiang et al. 2017). Cosmic reionization is

expected to proceed from high- to low-density regions (see Iliev et al. 2006; Ono et al. 2012; Overzier 2016). This reionization process is called the “inside-out” scenario. On the other hand, if major sources of cosmic reionization are X-ray-emitting objects like active galactic nuclei (AGNs), the scenario may be different. Due to the longer mean free path of X-ray photons compared to that of UV photons from galaxies and the slow hydrogen recombination rate in the low-density region, cosmic reionization would not originate from high-density but from low-density regions (see Miralda-Escudé et al. 2000; Nakamoto et al. 2001; McQuinn 2012; Mesinger et al. 2013). Although there are other intermediate scenarios between the scenarios above (e.g., Finlator et al. 2009), the physical process of cosmic reionization is tightly related to the major ionizing sources of cosmic reionization. Because observational evidence is limited (e.g., Matthee et al. 2018), identifying signatures of ionized bubbles around galaxy overdensity regions, if any, is key to testing the inside-out scenario of cosmic reionization.

Observations of galaxy overdensities near the epoch of cosmic reionization (EoR) are important for another reason. Standard structure formation models predict that a large fraction of high- $z$  galaxy overdensity regions evolve into massive galaxy clusters at  $z = 0$ . These galaxy overdensity regions are called protoclusters. A protocluster is often defined as a structure that is expected to collapse into a galaxy cluster with halo mass  $M_h > 10^{14} M_\odot$  (Chiang et al. 2013; Overzier 2016). In this paper, we use the same definition of protoclusters as that in Chiang et al. (2013) and Overzier (2016).<sup>15</sup> Galaxy overdensities at the EoR would be examples of first sites of galaxy cluster formation (e.g., Ishigaki et al. 2016).

Although the importance of high- $z$  galaxy overdensities is well recognized, only a few protoclusters at  $z \gtrsim 6$  have been reported to date (Ouchi et al. 2005; Utsumi et al. 2010; Toshikawa et al. 2012, 2018, 2014; Franck & McGaugh 2016a, 2016b; Chanchaiworawit et al. 2017). Protoclusters are commonly identified via the distributions of continuum-selected galaxies including dropout galaxies. However, it is difficult to find protoclusters using only continuum-selected galaxy samples, due to their large redshift uncertainties. Instead, one can use LAEs to identify protoclusters or galaxy overdensities in general, by exploiting the small redshift uncertainty of the LAEs, and the small velocity offsets between their systemic redshift and the one derived from Ly $\alpha$  (Shibuya et al. 2014). Here we investigate the LAE distribution and overdensity to identify protocluster candidates and to study the IGM ionization state around galaxy overdensities. The IGM ionization state is studied using the Ly $\alpha$  equivalent widths (EWs), which depend on  $x_{\text{H I}}$ , of LAEs (Dijkstra et al. 2011, 2016; Jensen et al. 2014; Kakiichi et al. 2016). Using a number of galaxy overdensities, we statistically investigate protoclusters and IGM ionization states.

In this paper, we identify protocluster candidates at  $z = 5.7$  and 6.6, based on the LAE samples of the Systematic Identification of LAEs for Visible Exploration and Reionization Research Using Subaru HSC (SILVERRUSH; Ouchi et al. 2018). SILVERRUSH is an ongoing research project based on the Subaru/Hyper Suprime-Cam (HSC) Subaru Strategic

Program (SSP; Furusawa et al. 2017; Miyazaki et al. 2017; Aihara et al. 2018a; Komiyama et al. 2018).

The SILVERRUSH project papers show the various properties of LAEs in the EoR: clustering (Ouchi et al. 2018), photometry (Shibuya et al. 2018a), spectroscopy (Shibuya et al. 2018b), Ly $\alpha$  LFs (Konno et al. 2018), ISM properties (Harikane et al. 2017), theoretical predictions (Inoue et al. 2018), and protoclusters (this work). This is the seventh publication in SILVERRUSH. SILVERRUSH is one of the twin programs devoted to the scientific results of high-redshift galaxies based on the HSC survey data. The other one is named the Great Optically Luminous Dropout Research Using Subaru HSC (GOLDRUSH; Harikane et al. 2018; Ono et al. 2018; Toshikawa et al. 2018). GOLDRUSH is related to dropout galaxies, which we need to refer to in order to conduct a complementary protocluster survey. Because we intend to enlarge our LAE samples, we include the LAE samples in Ouchi et al. (2008, 2010), which were previously obtained with Subaru/Suprime-Cam (SC; Miyazaki et al. 2002; see also Iye et al. 2004). We describe our photometric LAE samples using HSC and SC in Section 2. In Sections 3 and 4, we explain our spectroscopic LAE data and the theoretical models of Inoue et al. (2018), respectively. We present the list of protocluster candidates at  $z = 5.7$  and 6.6, and show the three-dimensional LAE distributions of protocluster candidates (Section 5). In Section 5, we also discuss the physical process of cosmic reionization using the LAE distributions.

Throughout this paper, we use the cosmological parameter set of  $\Omega_m = 0.3$ ,  $\Omega_\Lambda = 0.7$ ,  $\Omega_b = 0.04$ , and  $H_0 = 70 \text{ km s}^{-1} \text{ Mpc}^{-1}$ . The magnitudes are in the AB system.

## 2. Data and Samples

### 2.1. Photometric Samples of HSC-SSP Data

We calculate the galaxy overdensity and identify protocluster candidates using photometric LAE samples of HSC-SSP data. In our study, we use the two-narrowband (*NB816* and *NB921*) and five-broadband (*grizy*) imaging data of the HSC-SSP survey (Section 1) starting in 2014 March. The HSC-SSP survey is an ongoing program, with 300 nights allocated over 5 yr. It has three layers, UltraDeep, Deep, and Wide, with planned total survey areas of  $\sim 4 \text{ deg}^2$ ,  $\sim 30 \text{ deg}^2$ , and  $\sim 1400 \text{ deg}^2$ , respectively. The narrowband data are taken only in the UltraDeep and Deep layers. We use the early data sets of the HSC-SSP survey taken until 2016 April. The early data sets correspond to HSC-SSP S16A data (Aihara et al. 2018b). In these data sets, HSC SSP obtained *NB816* data in two fields of the UltraDeep layer, UD-SXDS and UD-COSMOS, and in two fields of the Deep layer, D-ELAIS-N1 and D-DEEP2-3. The data of *NB921* were taken in two fields of the UltraDeep layer, UD-SXDS and UD-COSMOS, and in three fields of the Deep layer, D-ELAIS-N1, D-DEEP2-3, and D-COSMOS. The  $5\sigma$  limiting magnitudes of the HSC imaging data are typically  $\simeq 25\text{--}25.5 \text{ mag}$  in the narrow bands and  $\simeq 26\text{--}27 \text{ mag}$  in the broad bands (Table 1; see also Shibuya et al. 2018a). The total survey areas of the early data sets are  $13.8 \text{ deg}^2$  and  $21.2 \text{ deg}^2$  in the fields with *NB816* and *NB921* data, respectively (Table 1). The *NB816* and *NB921* data allow us to identify strong Ly $\alpha$  emission lines of LAEs redshifted to  $z = 5.726 \pm 0.046$  and  $z = 6.580 \pm 0.056$ , respectively, where the redshift ranges are defined with the FWHMs of the narrow bands. The total survey volumes for the early data sets

<sup>15</sup> For details, see Section 5.1.3.

**Table 1**  
HSC Imaging Data

Layer (1)	Field (2)	Total Area (3)	Effective Area (4)	$g$ (5)	$r$ (6)	$i$ (7)	$z$ (8)	$y$ (9)	$NB816$ (10)	$NB921$ (11)
UD	SXDS	1.931 (2.016)	1.928 (1.873)	26.9	26.4	26.3	25.6	24.9	25.5	25.5
UD	COSMOS	1.965 (2.041)	1.965 (1.999)	26.9	26.6	26.2	25.8	25.1	25.7	25.6
Deep	COSMOS	...(5.345)	...(3.669)	26.5	26.1	26.0	25.5	24.7	...	25.3
Deep	ELAIS-N1	5.566 (6.053)	5.566 (5.599)	26.7	26.0	25.7	25.0	24.1	25.3	25.3
Deep	DEEP2-3	4.339 (5.735)	4.339 (3.100)	26.6	26.2	25.9	25.2	24.5	25.2	24.9

**Note.** (1) Layer, (2) field, (3) total survey area for the  $NB816$  ( $NB921$ ) data ( $\text{deg}^2$ ), (4) effective area of the  $NB816$  ( $NB921$ ) data used for the overdensity analysis ( $\text{deg}^2$ ), (5)–(11)  $5\sigma$  limiting magnitudes of the HSC  $g$ ,  $r$ ,  $i$ ,  $z$ ,  $y$ ,  $NB816$ , and  $NB921$  images in a circular aperture with a diameter of  $1''.5$  (mag).

**Table 2**  
Photometric Samples of the  $z = 5.7$  and  $6.6$  LAEs

Layer (1)	Field (2)	$z = 5.7$			$z = 6.6$		
		$NB816$ Full (3)	$NB816 < 24.5$ (4)	$NB816 < 25.0$ (5)	$NB921$ Full (6)	$NB921 < 24.5$ (7)	$NB921 < 25.0$ (8)
UD	SXDS	224	83	164	58	21	43
UD	COSMOS	201	52	123	338	31	82
Deep	COSMOS	... <sup>a</sup>	... <sup>a</sup>	... <sup>a</sup>	244	91	196 (135 <sup>b</sup> )
Deep	ELAIS-N1	229	140	166	349	142	258
Deep	DEEP2-3	423	127	319	164	104	82
Total		1077	402 <sup>c</sup>	772	1153	389	661 (600 <sup>b,c</sup> )

**Notes.** (1) Layer; (2) field; (3) number of  $z = 5.7$  LAEs in the HSC photometric sample; (4)–(5) same as (3), but for the  $z = 5.7$  LAEs that are brighter than 24.5 and 25.0 mag in the  $NB816$  band; (6) number of  $z = 6.6$  LAEs in the HSC photometric sample; (7)–(8) same as (6), but for the  $z = 6.6$  LAEs that are brighter than 24.5 and 25.0 mag in the  $NB921$  band.

<sup>a</sup> The  $NB816$  image is not taken in Deep COSMOS.

<sup>b</sup> Number of LAEs after the removal of the LAEs overlapping with those of UD COSMOS.

<sup>c</sup> Number of LAEs used for our overdensity measurements.

are  $1.2 \times 10^7 \text{ Mpc}^3$  at  $z = 5.7$  and  $1.9 \times 10^7 \text{ Mpc}^3$  at  $z = 6.6$ . Note that these survey volumes are  $\sim 2$ – $50$  and  $\sim 4$ – $100$  times larger than those of previous studies for LAEs at  $z = 5.7$  (e.g., Ouchi et al. 2008; Santos et al. 2016) and  $z = 6.6$  (e.g., Ouchi et al. 2010; Kashikawa et al. 2011; Matthee et al. 2015), respectively. They are also  $\sim 1000$  times larger than those of MUSE deep fields (e.g., Drake et al. 2017) and  $\sim 10$  times larger than those of the observation with  $NB816$  by SC4K (e.g., Sobral et al. 2018).

The data sets are reduced by the HSC-SSP Collaboration with `hscPipe` (Bosch et al. 2017). `hscPipe` is a pipeline based on the Large Synoptic Survey Telescope (LSST) pipeline (Ivezic et al. 2008; Axelrod et al. 2010; Jurić et al. 2015). The astrometry and photometry of the data sets are calibrated based on the Panoramic Survey Telescope and Rapid Response System (Pan-STARRS) 1 imaging survey (Schlafly et al. 2012; Tonry et al. 2012; Magnier et al. 2013).

Our photometric samples of  $z = 5.7$  and  $6.6$  LAEs are made by combining the narrowband color excess and the UV continuum break (Shibuya et al. 2018a). We apply color selection criteria similar to those of Ouchi et al. (2008, 2010), who studied  $z = 5.7$  and  $6.6$  LAEs, respectively with SC. The color selection criteria for the objects in the HSC data sets are defined as

$$i - NB816 \geq 1.2 \text{ and } g > g_{3\sigma} \text{ and} \\ [(r \leq r_{3\sigma} \text{ and } r - i \geq 1.0) \text{ or } (r > r_{3\sigma})] \quad (1)$$

and

$$z - NB921 \geq 1.0 \text{ and } g > g_{3\sigma} \text{ and } r > r_{3\sigma} \text{ and} \\ [(z \leq z_{3\sigma} \text{ and } i - z \geq 1.0) \text{ or } (z > z_{3\sigma})] \quad (2)$$

for  $z = 5.7$  and  $6.6$  LAEs, respectively (see Shibuya et al. 2018a). These color criteria are chosen to select LAEs with  $\text{Ly}\alpha$  EWs more than  $10$  ( $14$ )  $\text{\AA}$  in the rest frame at  $z = 5.7$  ( $6.6$ ; Shibuya et al. 2018a). We find 1077  $z = 5.7$  LAEs and 1153  $z = 6.6$  LAEs by photometry (Table 2). Shibuya et al. (2018b) took spectra of 18 LAEs in the photometric samples, and confirmed 13 LAEs at  $z = 5.7$  and  $6.6$  by spectroscopy. Because the LAEs include faint sources that might not have an identifiable signal with the depth of the spectroscopy, the contamination rate indicated by the spectroscopy is estimated to be 0%–30% in the  $z = 5.7$  and  $6.6$  LAEs in the photometric samples (see also Shibuya et al. 2018a, 2018b).

## 2.2. Photometric Samples of the SC Data

To select the spectroscopic targets of  $z = 5.7$  and  $6.6$  LAEs, we use the photometric samples of Ouchi et al. (2008, 2010), respectively, in addition to the HSC LAE samples in Section 2.1. Ouchi et al. (2008, 2010) have carried out narrowband imaging with SC in 2003 and 2005–2007, respectively. The total areas of the narrowband imaging are  $\sim 1 \text{ deg}^2$  and  $\sim 0.9 \text{ deg}^2$  for  $NB816$  and  $NB921$  images, respectively. Ouchi et al. (2008, 2010) detected objects in each narrowband image with SExtractor (Bertin & Arnouts 1996), and obtained SC LAE samples using color

**Table 3**  
Spectroscopic Observations

Layer (1)	Field (2)	Mask ID (3)	Date (4)	Total Exposure (5)	$N_{\text{LAE}}$ (6)	Grism (7)	CW (8)	Filter (9)
Keck/DEIMOS								
UD	SXDS	SXDS03	2010 Feb 11	3500	16	830	7900	OG550
Magellan/IMACS								
UD	SXDS	sxds1_07	2007 Nov 12	15600	4	Gri-150-18.8	...	GG455
UD	SXDS	sxds3r07	2007 Nov 13–14	35400	15	Gri-150-18.8	...	OG570
UD	SXDS	sxds5s08	2008 Nov 29	15300	22	Gri-300-26.7	...	WB6300-9500
UD	SXDS	sxds3s08	2008 Nov 30	15300	27	Gri-300-26.7	...	WB6300-9500
UD	SXDS	sxds2a08	2008 Dec 1	16200	22	Gri-300-26.7	...	WB6300-9500
UD	SXDS	sxds4a08	2008 Dec 2	18000	12	Gri-300-26.7	...	WB6300-9500
UD	SXDS	sxds1u08	2008 Dec 18–19	25200	11	Gri-300-26.7	...	WB6300-9500
UD	SXDS	sxds3a09	2009 Oct 11	21600	26	Gri-300-26.7	...	WB6300-9500
UD	SXDS	sxds2a09	2009 Oct 12	15300	16	Gri-300-26.7	...	WB6300-9500
UD	SXDS	oct2008_nb1190a <sup>a</sup>	2008 Oct 20–23	20700	9	Gri-300-26.7	...	WB6300-9500
UD	SXDS	oct2008_nb1190b <sup>a</sup>	2008 Oct 20–23	19800	4	Gri-300-26.7	...	WB6300-9500
UD	SXDS	oct2008_nb1190c <sup>a</sup>	2008 Oct 20–23	16200	8	Gri-300-26.7	...	WB6300-9500
UD	SXDS	oct2008_nb1190d <sup>a</sup>	2008 Oct 20–23	16200	11	Gri-300-26.7	...	WB6300-9500
UD	SXDS	sep2009_sxdsw1 <sup>a</sup>	2009 Sep 20	12600	1	Gri-300-26.7	...	WB6300-9500
UD	SXDS	sep2009_sxdsw2 <sup>a</sup>	2009 Sep 20	12600	3	Gri-300-26.7	...	WB6300-9500
UD	COSMOS	cos01_08	2008 Nov 29–Dec 2	21600	7	Gri-300-26.7	...	WB6300-9500
UD	COSMOS	cos02_08	2008 Dec 18–20	27900	5	Gri-300-26.7	...	WB6300-9500

**Note.** (1) Layer, (2) field, (3) mask ID, (4) date of observations, (5) total exposure time (s), (6) numbers of the observed LAEs, (7) disperser name, (8) central wavelength of the grating setting (Å), (9) filter name.

<sup>a</sup> See also Lee et al. (2012) and Momcheva et al. (2013).

selection criteria similar to Equations (1) and (2), defined as

$$i' - NB816 \geq 1.2 \text{ and } B > B_{2\sigma} \text{ and } V > V_{2\sigma} \text{ and} \\ [(R \leq R_{2\sigma} \text{ and } R - i' \geq 1.0) \text{ or } (R > R_{2\sigma})] \quad (3)$$

and

$$z' - NB921 \geq 1.0 \text{ and } B > B_{2\sigma} \text{ and } V > V_{2\sigma} \text{ and} \\ [(z' \leq z'_{3\sigma} \text{ and } i' - z' \geq 1.3) \text{ or } (z' > z'_{3\sigma})] \quad (4)$$

for  $z = 5.7$  and  $6.6$  LAEs, respectively. Ouchi et al. (2008, 2010) applied these selection criteria, and found 401 and 207 LAEs at  $z = 5.7$  and  $6.6$ , respectively. Ouchi et al. (2008, 2010) have estimated the contamination rates of the SC samples at  $z = 5.7$  and  $6.6$  to be  $\simeq 0\%$ – $25\%$  and  $0\%$ – $30\%$ , respectively. Note that we include other unreliable LAE candidates from Ouchi et al. (2008) in the spectroscopic targets.

Comparing the SC samples with the HSC samples, one will recognize that many LAEs in the SC samples are not included in the HSC samples. This is because the SC samples have faint LAEs down to the narrowband magnitudes of  $\sim 26$  mag, while the depth of the HSC samples only reaches  $\sim 25$  mag. Shibuya et al. (2018a) have estimated the matching rate between HSC samples and SC samples. They suggested that the matching rate is  $\simeq 70\%$  at  $\lesssim 24.5$  mag in narrow bands, although the rate is higher at a brighter magnitude.

### 3. Spectroscopic Observations and Samples

We conduct spectroscopic observations for the HSC and SC LAE samples. The spectroscopic observations for the HSC samples are presented in Shibuya et al. (2018b). Here we explain our spectroscopy for the SC samples that were conducted in 2007–2010 (Table 3).

#### 3.1. Keck/DEIMOS Observation

We carried out spectroscopic follow-up observations for our  $z = 5.7$  LAEs with the Deep Imaging Multi-Object Spectrograph (DEIMOS; Faber et al. 2003) on 2010 February 11. The sky was clear during the observations, and the seeing was  $\sim 0''.5$ . We observed 22 out of the 401 SC LAEs at  $z = 5.7$  (Ouchi et al. 2008), including very faint LAE candidates, and obtained 16 spectra in good condition. During the observations, we took the standard stars G191B2B for the flux calibration. We used a mask with a slit width of  $1''$ , the OG550 filter, and the 830 lines  $\text{mm}^{-1}$  grating that is blazed at  $8640 \text{ \AA}$ . The grating was tilted to be placed at a central wavelength of  $7900 \text{ \AA}$  on the detectors. The spectral coverage and the spectral resolution were  $4100\text{--}9400 \text{ \AA}$  and  $\lambda/\Delta\lambda \simeq 2400$ , respectively. We perform the data reduction using the spec2d IDL pipeline developed by the DEEP2 Redshift Survey Team (Davis et al. 2003). The central wavelengths of the  $\text{Ly}\alpha$  emission were determined by Gaussian fitting. We detected 15 out of the 16 LAEs, and obtained  $\text{Ly}\alpha$  line redshifts. The spectra of the example LAEs are shown in Figure 1.

#### 3.2. Magellan/IMACS Observation

We conducted follow-up spectroscopy for 425 objects selected from the samples of  $z = 5.7$  and  $z = 6.6$  LAEs in Ouchi et al. (2008, 2010), respectively. The observations were performed with the Inamori Magellan Areal Camera and Spectrograph (IMACS; Dressler et al. 2006) on the Magellan I Baade Telescope on 2007 November 12–14, 2008 November 29–December 2, 2008 December 18–19, and 2009 October 11–12. We chose the GG455 filter and the Gri-150-18.8 grism on 2007 November 12. In 2007 November 13–14, we change the filter from GG455 to OG570. For the rest of the IMACS

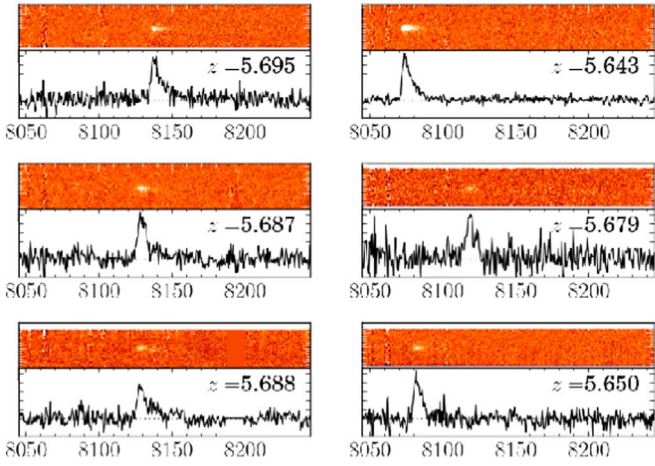


**Figure 1.** Examples of the  $z = 5.7$  LAE spectra obtained by our Keck/DEIMOS observations. The two- and one-dimensional spectra are shown in the top and bottom subpanels, respectively, in each panel. The  $x$ -axis represents the observed wavelength.

observations, we used the WB6300-9500 filter and the Gri-300-26.7 grism. The exposure time ranges from 15,300 to 35,400 s with seeing sizes of  $0''.5$ – $0''.8$ . We used a  $0''.8$  slit width that gives a spectral resolution of 1000–2000. We performed data reduction with the Carnegie Observatories System for Multi-Object Spectroscopy (COSMOS) pipeline, and detected Ly $\alpha$  emission lines around 8160 Å (9210 Å) for 130 (22) objects. Spectra of the example LAEs are shown in Figures 2–3.

### 3.3. Spectroscopic Samples and Catalogs

To add to the SC spectroscopic sample of the LAEs confirmed with DEIMOS and IMACS in Sections 3.1 and 3.2 and the HSC spectroscopic sample of Shibuya et al. (2018b) that includes LAEs in Ouchi et al. (2010), Sobral et al. (2015), and Hu et al. (2016), we use the redshift catalogs for the spectroscopically confirmed LAEs at  $z = 5.7$  (6.6) taken from Ouchi et al. (2005, 2008), Mallery et al. (2012), Chanchaiworawit et al. (2017), Guzmán et al. (2017), Jiang et al. (2017), and Jiang et al. (2018).

Note that, again, there are many LAEs in the SC spectroscopic sample that are not included in the HSC photometric sample. This is because the HSC photometric sample includes bright LAEs only down to  $\sim 25$  mag in a narrow band, while the SC samples (spectroscopic and photometric samples) have faint LAEs down to  $\sim 26$  mag in a narrow band (Section 2.2). Because the selection of the SC (and HSC) spectroscopic sample is heterogeneous, we use the homogeneous photometric sample of HSC LAEs to find protocluster candidates. The unified catalogs (the SC and HSC spectroscopic samples) are referred to for the confirmation of the redshifts of protocluster candidates in Section 5.1.4.

## 4. Theoretical Model

We compare our observational results with the cosmological simulation model of Inoue et al. (2018). Inoue et al. (2018) conducted  $N$ -body simulations in a box size of  $110 h^{-1}$  comoving Mpc (cMpc) length with  $512^3$  grids, which gives a spatial resolution of 214.8 comoving kpc. Inoue et al. (2018) presented models of three reionization histories depending on the ionizing emissivity of halos: early, mid, and late, all of which are consistent with the latest Thomson scattering optical

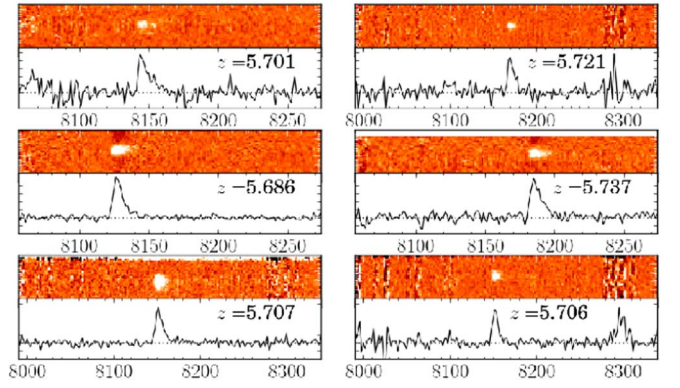


**Figure 2.** Same as Figure 1, but for our Magellan/IMACS spectra of the  $z = 5.7$  LAEs.

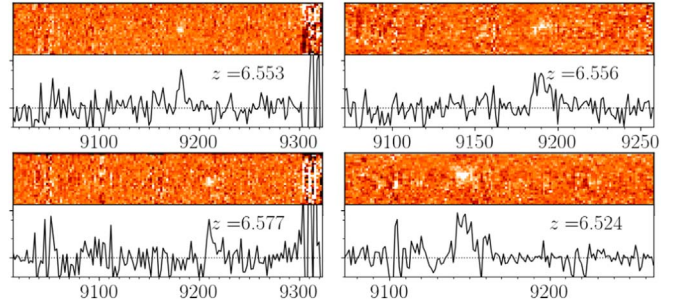


**Figure 3.** Same as Figure 1, but for our Magellan/IMACS spectra of the  $z = 6.6$  LAEs.

depth measurement (Planck Collaboration et al. 2016). Here we adopt the late model, which explains the recent neutral hydrogen fraction measurements at  $z \sim 6$ – $7$ . In the model, a total of  $4096^3$  dark matter particles are used with a mass resolution of  $7 \times 10^7 M_{\odot}$ . Inoue et al. (2018) performed numerical RT calculations to reproduce cosmic reionization. In this model, LAEs are created with the relation of the Ly $\alpha$  photon production rate and halo mass determined by the radiation hydrodynamics galaxy formation simulation of K. Hasegawa et al. (2017, in preparation). Inoue et al. (2018) assumed

$$L_{\text{Ly}\alpha, \text{int}} = 10^{42} \times (1 - e^{-10M_{\text{h},10}}) \times M_{\text{h},10}^{1.1} \times 10^{\delta_{\text{Ly}\alpha}} \text{ [erg s}^{-1}\text{]}, \quad (5)$$

where more massive halos produce more Ly $\alpha$  photons, due to the higher star-forming rate. Here,  $M_{\text{h},10}$  is the halo mass normalized by  $10^{10} M_{\odot}$ , and  $\delta_{\text{Ly}\alpha}$  represents the fluctuation of the Ly $\alpha$  photon production. The ISM Ly $\alpha$  escape fraction is defined as

$$f_{\text{esc},\alpha}^{\text{ISM}} = \exp(-\tau_{\alpha}), \quad (6)$$

where  $\tau_{\alpha}$  is the Ly $\alpha$  optical depth. Inoue et al. (2018) assumed the probability distribution of the Ly $\alpha$  optical depth as

$$P(\tau_{\alpha}) = \frac{\exp\{-(\tau_{\alpha} - \langle\tau_{\alpha}\rangle)^2/2\langle\tau_{\alpha}\rangle\}}{\sqrt{2\pi\langle\tau_{\alpha}\rangle}} \quad (7)$$

and

$$\langle\tau_{\alpha}\rangle = \tau_{\alpha,10} \left( \frac{M_{\text{h}}}{10^{10} M_{\odot}} \right)^p, \quad (8)$$

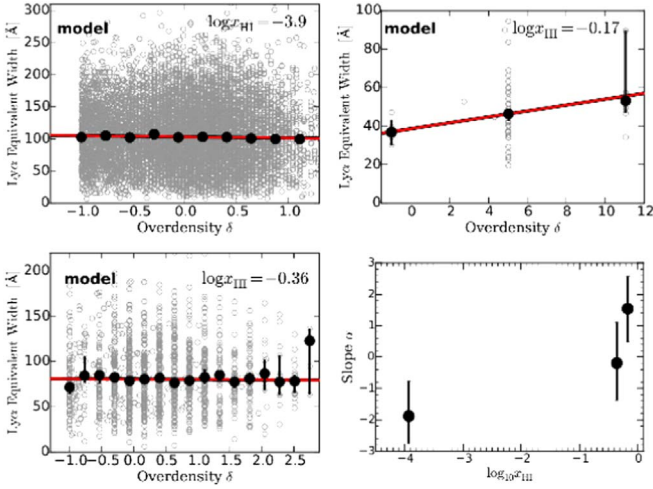


**Figure 4.**  $EW_{\text{Ly}\alpha}^{\text{rest}}$  as a function of  $\delta$  at  $\log_{10} x_{\text{HI}} = -3.9$  (upper left panel, corresponding to  $z = 5.7$ ),  $\log_{10} x_{\text{HI}} = -0.36$  (lower left panel, corresponding to  $z = 6.6$ ), and  $\log_{10} x_{\text{HI}} = -0.17$  (upper right panel, corresponding to  $z = 7.3$ ) in the model of Inoue et al. (2018). The values of  $\delta$  and  $EW_{\text{Ly}\alpha}^{\text{rest}}$  are shown with the gray open circles. The black filled circles and the bars indicate the median values and the error bars, respectively. The red line represents the best-fit linear function. The lower right panel shows the slope  $\alpha$  of the  $EW_{\text{Ly}\alpha}^{\text{rest}} - \delta$  relation as a function of  $x_{\text{HI}}$ , which is derived from the model of Inoue et al. (2018).

where  $p$  indicates the halo mass dependence of  $\langle \tau_{\alpha} \rangle$ . Inoue et al. (2018) calibrated the parameter  $\tau_{\alpha,10}$  with the  $z = 5.7$  Ly $\alpha$  LF (Konno et al. 2018), and compared the model predictions with the various observational quantities of the Ly $\alpha$  LFs at  $z = 6.6$  and  $7.3$  (Konno et al. 2014, 2018), the LAE angular autocorrelation functions at  $z = 5.7$  and  $6.6$  (Ouchi et al. 2018), and the LAE fractions in Lyman break galaxies at  $z = 5-7$  (Stark et al. 2011; Ono et al. 2012). In this paper, we use the model with the best parameter set ( $\delta_{\text{Ly}\alpha} = 0$ ,  $p = 1/3$ , and  $\tau_{\alpha,10} = 1.1$ ) concluded by Inoue et al. (2018).

We select mock LAEs brighter than the  $10^{42.5}$  erg s $^{-1}$  from the observed Ly $\alpha$  luminosity that escaped through the IGM. Hereafter, we call these mock LAEs ‘‘LAE all.’’ We obtain 9574, 1415, and 55 mock LAEs at  $z = 5.7$ ,  $6.6$ , and  $7.3$ , respectively, from the entire simulation box of the model.

For comparison with our observational results, we calculate the overdensity  $\delta$  of the mock LAEs, which is defined as

$$\delta = \frac{n - \bar{n}}{\bar{n}}, \quad (9)$$

where  $n$  ( $\bar{n}$ ) is the total (average) number of LAEs found in a cylindrical volume that mimics the observational volume for the  $\delta$  measurements (Section 5.1.1). We choose the height of  $\sim 40$  cMpc for the cylinder that corresponds to the redshift range of the narrowband-observation LAE selection. The base area of the cylinder is defined by a radius of  $\sim 10$  cMpc, which is the typical size of protoclusters assumed in Chiang et al. (2013) and Lovell et al. (2017). The volume of the cylinder is  $\sim 1 \times 10^4$  cMpc $^3$ . Note that  $\delta$  would be discrete when  $\bar{n}$  is small. Figure 4 shows the relations between the Ly $\alpha$  rest-frame equivalent width  $EW_{\text{Ly}\alpha}^{\text{rest}}$  and  $\delta$  in Inoue et al. (2018) for a universe with neutral hydrogen fractions of  $\log_{10} x_{\text{HI}} = -3.9$ ,  $-0.36$ , and  $-0.17$ , which are the average values of the simulation boxes at  $z = 5.7$ ,  $6.6$ , and  $7.3$ , respectively.

Inoue et al. (2018) derived  $EW_{\text{Ly}\alpha}^{\text{rest}}$  as

$$EW_{\text{Ly}\alpha}^{\text{rest}} = \frac{L_{\text{Ly}\alpha, \text{int}}^{\text{ISM}} T_{\text{Ly}\alpha}^{\text{IGM}}}{L_{\lambda_{\alpha}}^{\text{con}}}, \quad (10)$$

where  $T_{\alpha}^{\text{IGM}}$  and  $L_{\lambda_{\alpha}}^{\text{con}}$  are the IGM transmission for Ly $\alpha$  photons and the continuum flux density at the Ly $\alpha$  wavelength  $\lambda_{\alpha}$ , respectively. The relations of  $EW_{\text{Ly}\alpha}^{\text{rest}} - \delta$  are fit with a linear function,  $EW_{\text{Ly}\alpha}^{\text{rest}} = \alpha \delta + EW_{\delta=0}$ , where  $\alpha$  and  $EW_{\delta=0}$  are the slope and the  $EW_{\text{Ly}\alpha}^{\text{rest}}$  value at  $\delta = 0$ , respectively. The lower right panel of Figure 4 shows  $\alpha$  as a function of  $x_{\text{HI}}$  obtained by the model calculations. The slope  $\alpha$  increases from the post-reionization epoch ( $\log_{10} x_{\text{HI}} = -3.9$ ) to the EoR ( $\log_{10} x_{\text{HI}} = -0.36$  and  $-0.17$ ). In the inside-out scenario of cosmic reionization,  $EW_{\text{Ly}\alpha}^{\text{rest}}$  values at high-overdensity regions would be higher than those at lower overdensity regions. This is because the Ly $\alpha$  escape fraction is higher inside the ionized bubbles than outside the ionized bubbles. Thus, if cosmic reionization proceeds in an inside-out manner, the slope  $\alpha$  is high at the EoR.

## 5. Results and Discussion

### 5.1. Spatial Distribution of LAEs

#### 5.1.1. Overdensity Measurements

We calculate the LAE overdensities in each field with the HSC LAE samples, although there are different methods for measuring overdensities (e.g., Darvish et al. 2015). The definition of the LAE overdensity for our observational data is the same as the one for the model shown in Equation (9). We use a cylinder with a radius of  $0^{\circ}07$  (10 cMpc at  $z \sim 6$ ) in the same manner as in Section 4. The height of the cylinder along a line of sight is 40 cMpc, the same as the width of the redshift distribution of the HSC LAEs. The volume of the cylinder is  $\sim 1 \times 10^4$  cMpc $^3$ , same as in Section 4. Because some regions of the HSC narrowband data are not deep enough to calculate  $\delta$ , due to the data quality, we should not use the HSC LAEs found in the shallow regions for the density evaluation. The HSC imaging data are divided into  $1.7 \times 1.7$  deg $^2$  rectangular tracts that are made of  $0.2 \times 0.2$  deg $^2$  rectangular patches. We estimate the  $5\sigma$  limiting magnitude of each patch in the NB816 (NB921) data for the  $z = 5.7$  (6.6) LAEs. We evaluate  $\delta$  only in patches where the  $5\sigma$  limiting magnitude of the NB816 (NB921) band is deeper than 24.5 (25.0) mag to maintain a high-detection completeness of LAEs (Konno et al. 2018). These limiting magnitudes of NB816 and NB921 correspond to Ly $\alpha$  luminosity limits  $\sim 10^{43.0}$  and  $\sim 10^{42.8}$  erg s $^{-1}$ , respectively. We thus remove the data patches with  $5\sigma$  limiting magnitudes shallower than NB816 = 24.5 or NB921 = 25.0. We define these patches as ‘‘removed patches.’’ We also do not use the part of the D-COSMOS field that overlaps with the UD-COSMOS field. We find that 0.02% and 23% of the survey areas are removed in our samples of LAEs at  $z = 5.7$  and  $6.6$ , respectively. The effective areas used for the  $\delta$  calculations are 13.8 and 16.2 deg $^2$  for LAEs at  $z = 5.7$  and  $6.6$ , respectively (Table 1). The effective survey volumes used for the  $\delta$  calculations are  $1.1 \times 10^7$  Mpc $^3$  and  $1.5 \times 10^7$  Mpc $^3$  at  $z = 5.7$  and  $6.6$ , respectively. The number of LAEs at  $z = 5.7$  (6.6) in the effective area is 402 (600). We assume that the number density of LAEs in the masked regions is the same as the mean

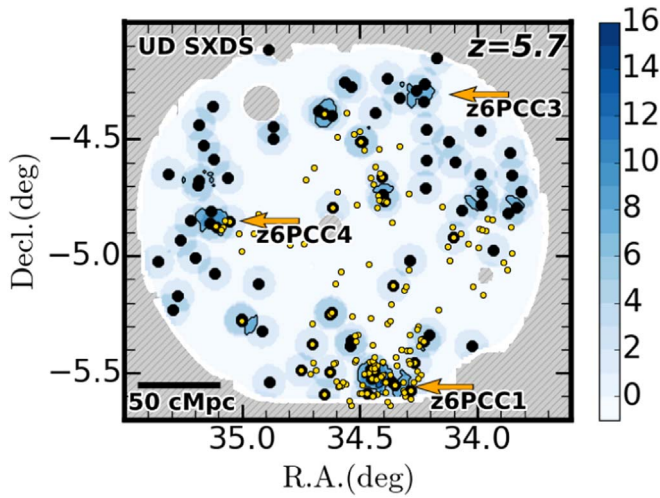


**Figure 5.** Sky distribution of the  $z = 5.7$  LAEs (black filled circles) with the surface overdensity contours (black lines) in the NB816 UD-SXDS field. The black line contours correspond to  $\delta = 5\text{--}15$  with a step of  $\Delta\delta = 5$ . Higher density regions are shown with bluer colors. The yellow filled circles represent spectroscopically confirmed LAEs. Masked regions and removed patches are presented as gray regions. See also Higuchi et al. (2019).

number density of LAEs in all fields. We also do not evaluate  $\delta$  for a cylinder, in which more than 50% of the area is masked. We show the HSC LAE sky distribution and the overdensity maps at  $z = 5.7$  and 6.6 in Figures 5–12. Note that the peak of the overdensity is not always centered at the highest density region. This is because the position of the peak has an uncertainty on a scale of  $0^{\circ}07$ .

### 5.1.2. Overdensity Identifications

We find that  $\delta$  values of the HSC LAEs in some regions significantly exceed those expected from a random distribution. Here, a high-density region (HDR) is defined as a region that has at least four LAEs in a radius of  $0^{\circ}07$ . This criterion of HDR corresponds to  $\delta = 9.7$  (6.6) at  $z = 5.7$  (6.6). Having this criterion, we find 14 (25) HDRs at  $z = 5.7$  (6.6). We conduct Monte Carlo simulations to estimate how many HDRs are found by chance for randomly distributed sources. We generate randomly distributed mock LAEs with number density and survey area the same as those of our LAE samples, 402 (600) LAEs at  $z = 5.7$  (6.6) in the 13.8 (16.2)  $\text{deg}^2$  sky, and calculate  $\delta$ . We perform this calculation 100 times, and obtain the average number of HDRs that are found by chance. We find that the average number of HDRs that are found by chance in our observational data of LAEs at  $z = 5.7$  (6.6) is 8.2 (19.7). The number of HDRs (14, 25) found in our observations is larger than the one found by chance (8.2, 19.7) in the  $z = (5.7, 6.6)$  data. Defining the HDR effective number as the number of observationally found HDRs subtracted by the one of the Monte Carlo simulations, we calculate it to be  $\simeq 6$  (5) at  $z = 5.7$  (6.6). To present another sample of HDRs that has a lower chance of being selected by chance (a lower contamination rate) but has a lower completeness value, we also define ‘‘Secure HDR,’’ a region that has at least six LAEs in a radius of  $0^{\circ}07$ . We find two (seven) Secure HDRs at  $z = 5.7$  (6.6) as shown in Table 4. From the Monte Carlo simulations, we find that there are no Secure HDRs selected by chance. Although they might be contaminated by randomly distributed sources, we keep the selection criteria of HDRs to align with previous

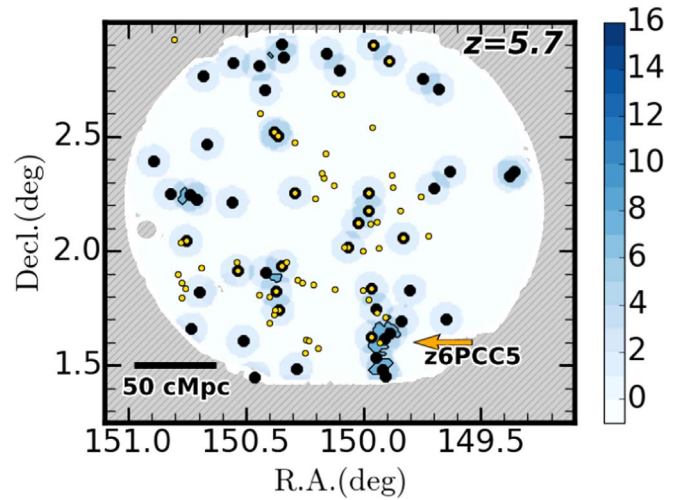


**Figure 6.** Same as Figure 5, but for the  $z = 5.7$  LAEs in the UD-COSMOS field.

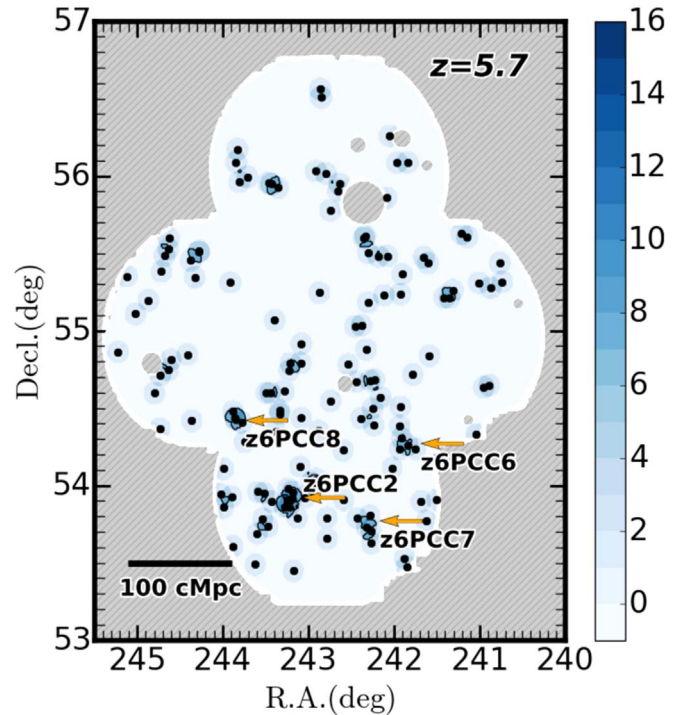


**Figure 7.** Same as Figure 5, but for the  $z = 5.7$  LAEs in the D-ELAIS-N1 field.

protocluster studies (Ouchi et al. 2005; Chanchaiworawit et al. 2017).

Here we discuss the results with the search radii different from  $0^{\circ}07$ . If we change the search radius, the descendants’ properties (such as today’s halo masses) become different, as suggested by theoretical simulations (Chiang et al. 2013). In other words, an HDR selection with a different search radius provides a physically different system. By this reason, one cannot directly compare the numbers of HDRs with different search radii. Nevertheless, we search for overdensities with a radius of  $0^{\circ}09$ , which is 30% larger than the original radius. In this case, we define HDRs as regions that contain  $>6.8$  ( $=4 \times (0.091/0.07)^2$ ) LAEs in a  $0^{\circ}09$  radius. We find one and three HDRs at  $z = 5.7$  and 6.6, respectively. Although the

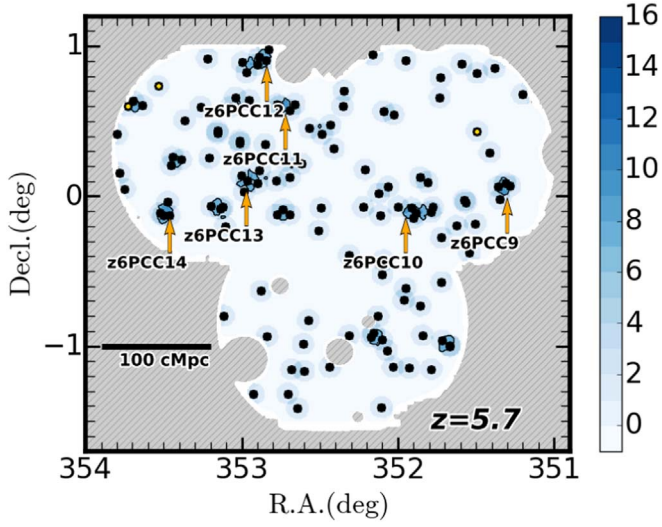


Figure 8. Same as Figure 5, but for the  $z = 5.7$  LAEs in the D-DEEP2-3 field.

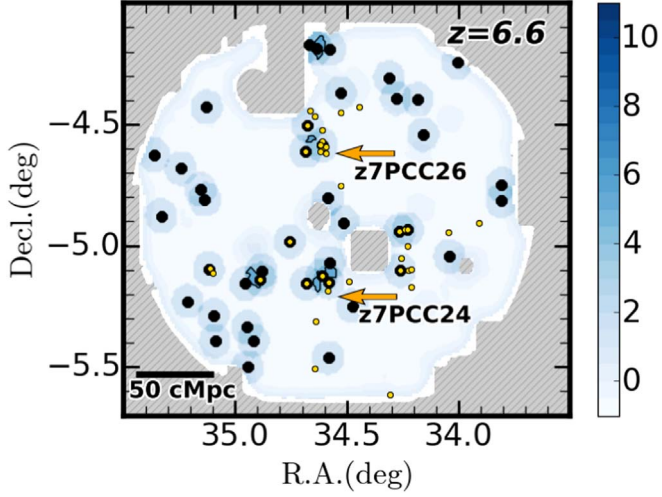


Figure 9. Same as Figure 5, but for the  $z = 6.6$  LAEs in the UD-SXDS field.

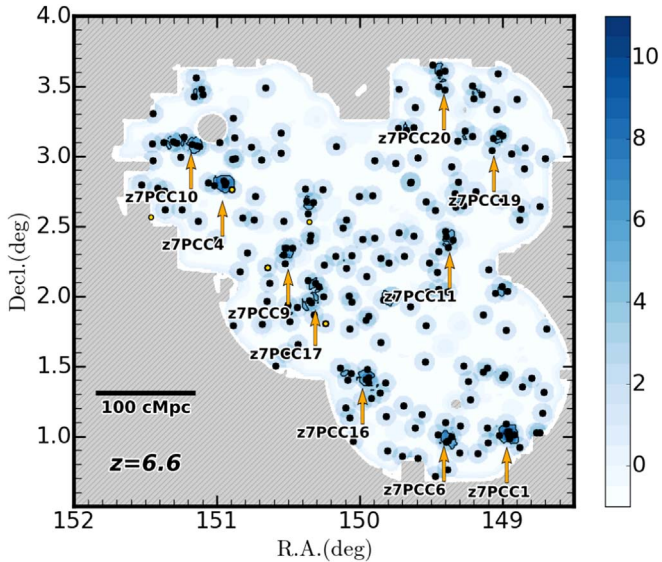


Figure 10. Same as Figure 5, but for the  $z = 6.6$  LAEs in the UD/D-COSMOS field.

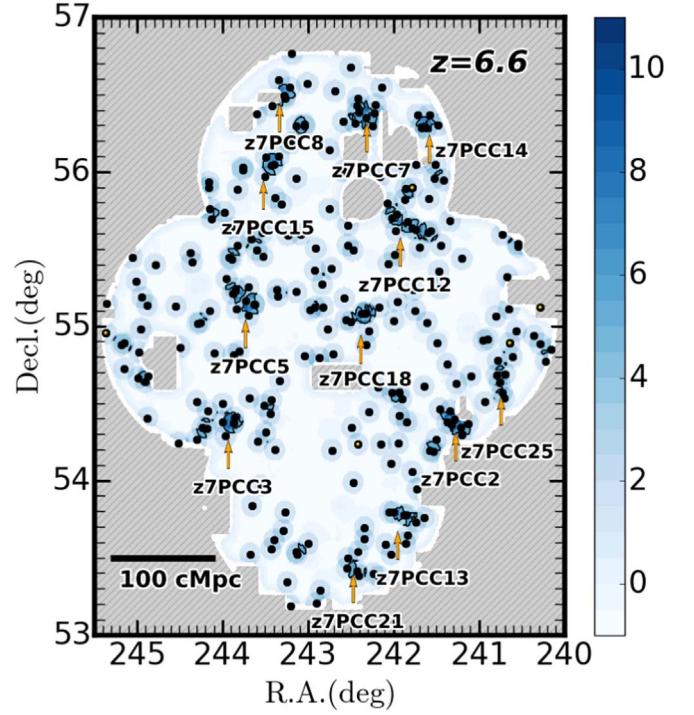


Figure 11. Same as Figure 5, but for the  $z = 6.6$  LAEs in the D-ELAIS-N1 field.

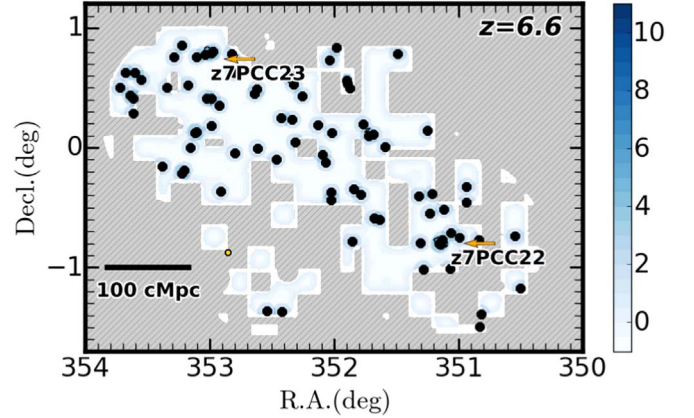


Figure 12. Same as Figure 5, but for the  $z = 6.6$  LAEs in the D-DEEP2-3 field.

numbers of HDRs are smaller than what we have found with a  $0^{\circ}07$  radius, all of these, 1 + 3, HDRs are included in our HDR sample (Table 4). We also calculate overdensities with a search radius of  $0^{\circ}05$  that is 30% smaller than the original radius. In this case, HDRs are defined as regions where  $>2.0$  ( $=4 \times (0.049/0.07)^2$ ) LAEs in a  $0^{\circ}05$  radius exist. We find 25 and 38 HDRs at  $z = 5.7$  and  $6.6$ , respectively. Based on Monte Carlo simulations performed in the same manner as described above, the number of HDRs that are selected by chance is 17.8 (33.5) at  $z = 5.7$  ( $6.6$ ), suggesting that the HDR effective number is  $\simeq 7$  (5), which is comparable with that of the  $0^{\circ}07$  radius result, i.e.,  $\simeq 6$  (5), obtained above.

There is an overdensity of  $z = 6.6$  LAEs at R.A. =  $34^{\circ}64$  and decl. =  $-4.56$ , whose  $\delta$  is 6.1, slightly below our criterion of HDR ( $\delta > 6.6$ ). This overdensity is reported by Chanchaiworawit et al. (2017). Although this overdensity does not meet our HDR criterion, we include this overdensity in our sample of HDRs. We thus obtain 14 and 26 HDRs at  $z = 5.7$  and  $6.6$ ,



**Table 4**  
Protocluster Candidates

Name (1)	Layer (2)	Field (3)	R.A. (J2000) (4)	Decl. (J2000) (5)	Overdensity $\delta$ (6)	$n_{\text{photo}}$ (7)	$n_{\text{photo}}^{\text{FULL}}$ (8)	$n_{\text{spec}}$ (9)	$\langle z_{\text{spec}} \rangle$ (10)	Secure (11)
$z = 5.7$										
HSC-z6PCC3	UD	SXDS	34.26	-4.32	$9.7^{+8.5}_{-5.1}$	4	5	0	...	No
HSC-z6PCC1	UD	SXDS	34.42	-5.54	$15.0^{+9.6}_{-6.4}$	6	7	13	5.679	Yes
HSC-z6PCC4	UD	SXDS	35.16	-4.85	$9.7^{+8.5}_{-5.1}$	4	7	4	5.722	No
HSC-z6PCC5	UD	COSMOS	149.94	1.60	$9.7^{+8.5}_{-5.1}$	4	5	2	5.686	No
HSC-z6PCC6	Deep	ELAIS-N1	241.84	54.27	$9.7^{+8.5}_{-5.1}$	4	4	0	...	No
HSC-z6PCC7	Deep	ELAIS-N1	242.32	53.77	$9.7^{+8.5}_{-5.1}$	4	5	0	...	No
HSC-z6PCC2	Deep	ELAIS-N1	243.22	53.92	$15.0^{+9.6}_{-6.4}$	6	8	0	...	Yes
HSC-z6PCC8	Deep	ELAIS-N1	243.89	54.42	$9.7^{+8.5}_{-5.1}$	4	4	0	...	No
HSC-z6PCC9	Deep	DEEP2-3	351.30	0.03	$9.7^{+8.5}_{-5.1}$	4	4	0	...	No
HSC-z6PCC10	Deep	DEEP2-3	351.95	-0.10	$9.7^{+8.5}_{-5.1}$	4	6	0	...	No
HSC-z6PCC11	Deep	DEEP2-3	352.72	0.60	$9.7^{+8.5}_{-5.1}$	4	4	0	...	No
HSC-z6PCC12	Deep	DEEP2-3	352.84	0.91	$9.7^{+8.5}_{-5.1}$	4	6	0	...	No
HSC-z6PCC13	Deep	DEEP2-3	352.97	0.08	$9.7^{+8.5}_{-5.1}$	4	4	0	...	No
HSC-z6PCC14	Deep	DEEP2-3	353.45	-0.10	$9.7^{+8.5}_{-5.1}$	4	4	0	...	No
$z = 6.6$										
HSC-z7PCC24	UD	SXDS	34.63	-5.11	$6.8^{+6.1}_{-3.7}$	4	4	3	6.574	No
HSC-z7PCC26	UD	SXDS	34.64	-4.56	$6.1^{+5.6}_{-3.1}$	3	3	6	6.537	No
HSC-z7PCC1	UD/Deep	COSMOS	148.96	1.02	$10.9^{+6.9}_{-4.6}$	6	6	0	...	Yes
HSC-z7PCC19	UD/Deep	COSMOS	149.05	3.10	$6.9^{+6.1}_{-3.7}$	4	4	0	...	No
HSC-z7PCC11	UD/Deep	COSMOS	149.36	2.41	$7.2^{+6.1}_{-3.7}$	4	4	0	...	No
HSC-z7PCC6	UD/Deep	COSMOS	149.40	1.03	$8.8^{+6.5}_{-4.1}$	5	5	0	...	Yes
HSC-z7PCC20	UD/Deep	COSMOS	149.40	3.54	$6.9^{+6.1}_{-3.7}$	4	4	0	...	No
HSC-z7PCC16	UD/Deep	COSMOS	149.97	1.44	$7.0^{+6.1}_{-3.7}$	4	6	0	...	No
HSC-z7PCC17	UD/Deep	COSMOS	150.3	2.00	$7.0^{+6.1}_{-3.7}$	4	6	0	...	No
HSC-z7PCC9	UD/Deep	COSMOS	150.49	2.29	$7.7^{+6.1}_{-3.7}$	4	7	0	...	No
HSC-z7PCC4	UD/Deep	COSMOS	150.95	2.78	$9.0^{+6.5}_{-4.1}$	5	5	1	6.575	Yes
HSC-z7PCC10	UD/Deep	COSMOS	151.17	3.12	$7.3^{+6.1}_{-3.7}$	4	2	0	...	No
HSC-z7PCC25	Deep	ELAIS-N1	240.74	54.63	$6.8^{+6.1}_{-3.7}$	4	4	0	...	No
HSC-z7PCC2	Deep	ELAIS-N1	241.27	54.40	$9.8^{+6.5}_{-4.1}$	5	5	0	...	Yes
HSC-z7PCC14	Deep	ELAIS-N1	241.58	56.33	$7.1^{+6.1}_{-3.7}$	4	4	0	...	No
HSC-z7PCC12	Deep	ELAIS-N1	241.92	55.66	$7.2^{+6.1}_{-3.7}$	4	7	0	...	No
HSC-z7PCC13	Deep	ELAIS-N1	241.95	53.76	$7.2^{+6.1}_{-3.7}$	4	4	0	...	No
HSC-z7PCC7	Deep	ELAIS-N1	242.31	56.40	$8.8^{+6.5}_{-4.1}$	5	5	0	...	Yes
HSC-z7PCC18	Deep	ELAIS-N1	242.38	55.03	$7.0^{+6.1}_{-3.7}$	4	4	0	...	No
HSC-z7PCC21	Deep	ELAIS-N1	242.47	53.48	$6.9^{+6.1}_{-3.7}$	4	4	0	...	No
HSC-z7PCC8	Deep	ELAIS-N1	243.33	56.53	$8.1^{+6.1}_{-3.7}$	4	4	0	...	No
HSC-z7PCC15	Deep	ELAIS-N1	243.52	56.03	$7.1^{+6.1}_{-3.7}$	4	5	0	...	No
HSC-z7PCC5	Deep	ELAIS-N1	243.73	55.13	$8.9^{+6.5}_{-4.1}$	5	5	0	...	Yes
HSC-z7PCC3	Deep	ELAIS-N1	243.93	54.35	$9.3^{+6.5}_{-4.1}$	5	5	0	...	Yes
HSC-z7PCC22	Deep	DEEP2-3	351.11	-0.76	$6.9^{+6.1}_{-3.7}$	4	4	0	...	No
HSC-z7PCC23	Deep	DEEP2-3	353.04	0.78	$6.9^{+6.1}_{-3.7}$	4	4	0	...	No

**Note.** (1) Object ID, (2) layer, (3) field, (4) R.A. of the center of the member LAEs (deg), (5) decl. of the center of the member LAEs (deg), (6) highest  $\delta$  in the protocluster candidates and its errors (Gehrels 1986), (7) number of LAEs with  $NB816 < 24.5$  ( $NB921 < 25.0$ ) within a radius of  $0^\circ 07'$  from the center of the protocluster candidate at  $z = 5.7$  (6.6). (8) same as (7), but for all of the HSC LAEs down to our detection limits, (9) number of the spectroscopically confirmed LAEs within a radius of 10 cMpc from the center of the protocluster candidates, (10) average redshift value of the spectroscopically confirmed LAEs, (11) Flag of Secure HDRs.

respectively. The number density of HDRs is  $1.2 \times 10^{-6}$  ( $1.7 \times 10^{-6}$ )  $\text{Mpc}^{-3}$  at  $z = 5.7$  (6.6).

### 5.1.3. Halo Mass Estimates

From the theoretical model of Inoue et al. (2018), we obtain the halo mass  $M_h$  as a function of overdensity  $\delta$ . Because the halo mass is strongly related to the structure formation tightly

connected with the abundance of halos and galaxies, we use LAEs in the model of Inoue et al. (2018) with abundance the same as those of the HSC LAEs. We define  $M_h$  as the most massive halo found in a cylindrical volume used for the  $\delta$  calculation. The upper (lower) panel of Figure 13 shows  $M_h$  as a function of  $\delta$  at  $z = 5.7$  (6.6). We fit the  $M_h$ - $\delta$  relation with a linear function and obtain  $\log_{10}[M_h/M_\odot] = 0.021\delta + 11.80$

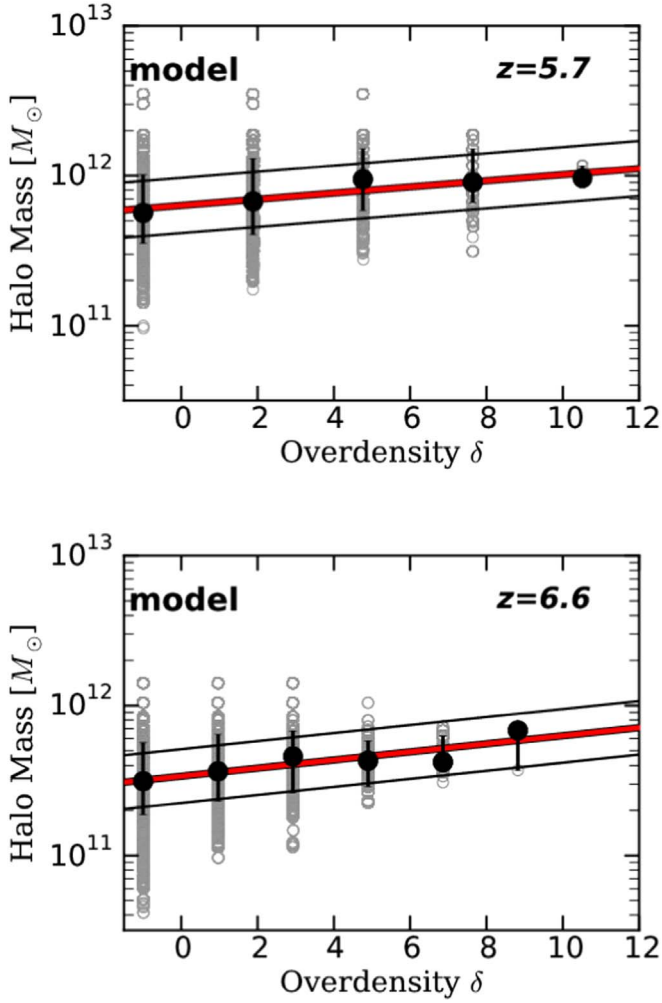


**Figure 13.** Halo mass as a function of overdensity  $\delta$  for the model LAEs (gray unfilled circles) produced in the model of Inoue et al. (2018) at  $z = 5.7$  (upper panel) and 6.6 (lower panel), respectively. The black filled circles with the error bars indicate the median values of the model LAEs. The red and black lines represent the best-fit linear function and the 68% distribution of the model LAEs.

( $\log_{10}[M_h/M_\odot] = 0.027\delta + 11.53$ ) at  $z = 5.7$  (6.6). We use the extended Press–Schechter model of Hamana et al. (2006) to estimate the present-day halo masses of the high- $z$  ( $z = 5.7$  and 6.6) halos. Based on the  $M_h$ – $\delta$  relation, we find that 60% (58%) of the  $z = 5.7$  (6.6)  $M_h$  halos in the HDRs are expected to evolve into present-day cluster halos with mass of  $>10^{14} M_\odot$  by  $z = 0$ . Because more than half of the  $M_h$  halos in the HDRs are progenitors of the present-day clusters, we regard the 14 (26) HDRs at  $z = 5.7$  (6.6) as protocluster candidates (e.g., Chiang et al. 2013; Overzier 2016). The 14 (26) protocluster candidates are listed in Table 4. Here, our  $z = 5.7$  (6.6) protocluster candidates are named “HSC- $z6PCC$ ” (“HSC- $z7PCC$ ”) followed by the identification number. Note that the identification number is given in order of  $\delta$  at each redshift.

We compare the abundance of the protocluster candidates with that of present-day clusters. The comoving survey volumes of the HSC observations are  $\sim 1.2 \times 10^7 \text{ Mpc}^3$  and  $\sim 1.9 \times 10^7 \text{ Mpc}^3$  at  $z = 5.7$  and 6.6, respectively. Because there exists one present-day cluster with a mass of  $1 - 3 \times 10^{14} M_\odot$  in a volume of  $\sim 5 \times 10^5 \text{ Mpc}^3$  (Reiprich & Böhringer 2002), it is expected that our survey volumes at  $z = 5.7$  and 6.6 include  $\sim 20$  and  $\sim 40$  present-day clusters,

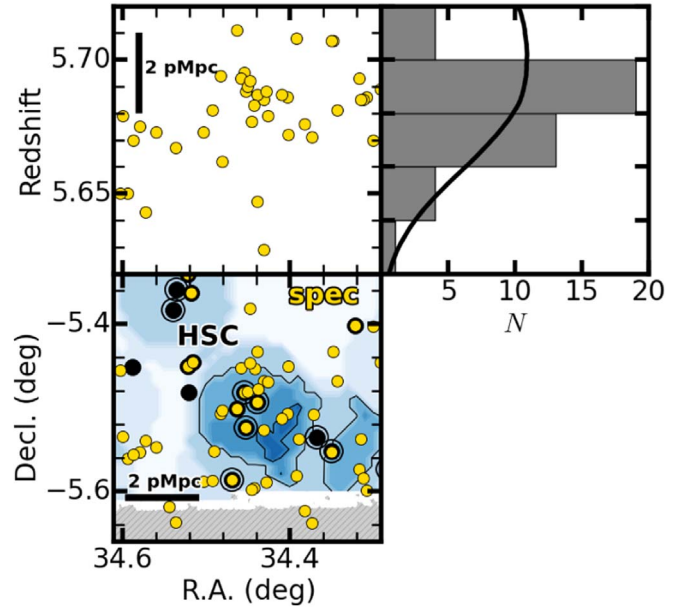


**Figure 14.** Three-dimensional map of HSC-z6PCC1. The bottom panel presents the distribution of the LAEs projected on the sky. The top-left panel shows the distribution of the LAEs on the plane of the transverse (east to west) versus radial (redshift) directions. The black filled circles represent our HSC LAEs. The symbols with an unfilled circle indicate our HSC LAEs with  $NB816 < 24.5$  that are used for the overdensity evaluation. The yellow filled circles denote the spectroscopically confirmed LAEs that include faint sources with  $NB816 \approx 25$ –26. The black line contours correspond to  $\delta = 5$ –15 with a step of  $\Delta\delta = 5$ . The masked regions are shown by the gray regions. The top right panel shows the redshift distribution of the spectroscopically confirmed LAEs. The black line indicates the mean expected number of LAEs in the region.

respectively. These numbers are comparable with those of our protocluster candidates, 14 and 26.

#### 5.1.4. Three-dimensional Distribution and Protocluster Candidates

Based on the follow-up spectroscopic observations in Section 3, we find three (three) protocluster candidates at  $z = 5.7$  (6.6) which have (a) spectroscopically confirmed LAE (s). These are HSC-z6PCC1, HSC-z6PCC4, and HSC-z6PCC5 (HSC-z7PCC4, HSC-z7PCC24, and HSC-z7PCC26) at  $z = 5.7$  (6.6). The three-dimensional distributions of HSC-z6PCC1, HSC-z6PCC4, HSC-z6PCC5, HSC-z7PCC24, and HSC-z7PCC26 are shown in Figures 14–18. Here we explain three examples of the protocluster candidates, HSC-z6PCC1, HSC-z7PCC24, and HSC-z7PCC26.

**HSC-z6PCC1:** HSC-z6PCC1 (Figure 14) consists of  $z = 5.7$  LAEs in the southern part of UD SXDS. Thirteen spectroscopically confirmed LAEs exist within a distance of  $\sim 1$  physical Mpc (pMpc). The redshift averaged over the spectroscopically confirmed LAEs is  $z = 5.679$ . HSC-z6PCC1 is the same structure as Clump A, which is a protocluster identified by Ouchi et al. (2005). Six out of the 12 spectroscopically confirmed LAEs are included in Clump A.

**HSC-z7PCC24:** HSC-z7PCC24 at  $z = 6.6$  (Figure 17) is located at the center of UD SXDS. HSC-z7PCC24 consists of five spectroscopically confirmed LAEs, including the giant Ly $\alpha$  nebula “Himiko” (Ouchi et al. 2009). The average redshift of the LAEs is  $z = 6.574$ . If all of the LAEs of HSC-z7PCC24 are spectroscopically confirmed, HSC-z7PCC24 could be one of the earliest protoclusters found to date.

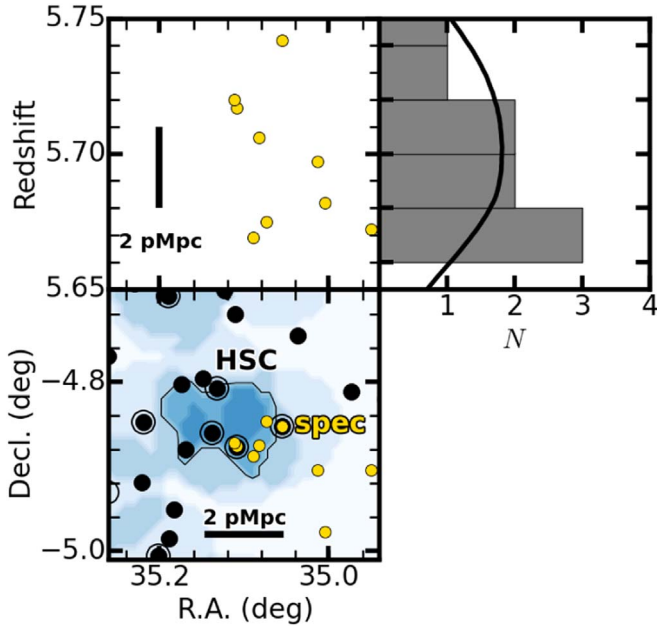


Figure 15. Same as Figure 14, but for HSC-z6PCC4.

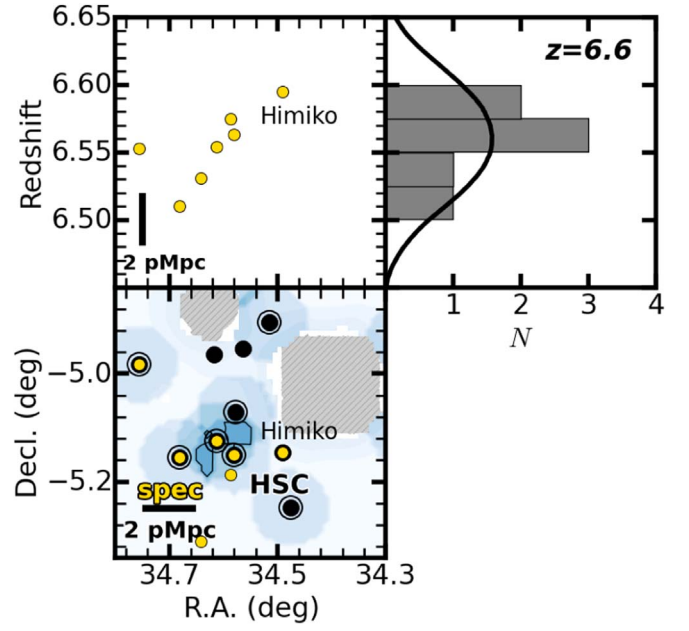


Figure 17. Same as Figure 14, but for HSC-z7PCC24. The symbols with an unfilled circle indicate our HSC LAEs with  $N_{B921} < 25.0$  that are used for the overdensity evaluation. The yellow circles indicate the spectroscopically confirmed LAEs including sources with  $N_{B921} \approx 25$ –26. See also Higuchi et al. (2019).

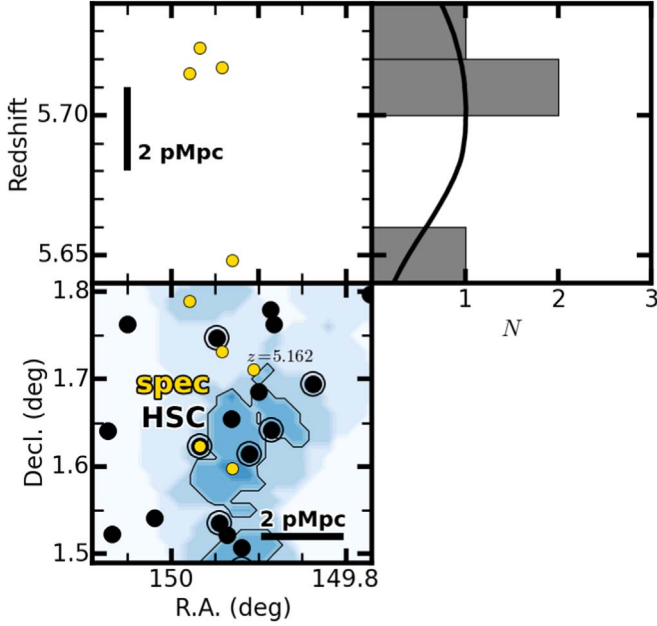


Figure 16. Same as Figure 14, but for HSC-z6PCC5.

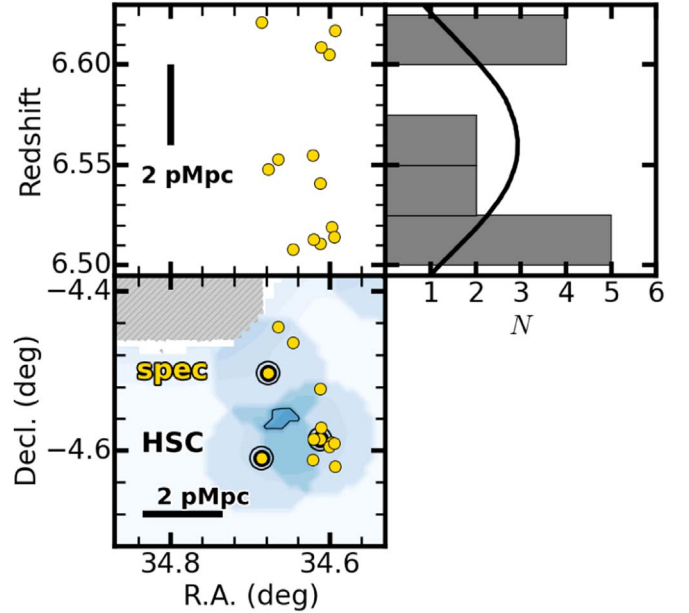


Figure 18. Same as Figure 17, but for HSC-z7PCC26.

**HSC-z7PCC26:** HSC-z7PCC26 (Figure 18) is placed at the northern part of UD SXDS at  $z = 6.6$ . This is the protocluster candidate reported by Chanchaiworawit et al. (2017), although the overdensity of HSC-z7PCC26 is  $\delta = 6.1$ , slightly below our criterion of protocluster candidates (Section 5.1.2). There are six spectroscopically confirmed LAEs in a sphere with a radius of  $\sim 1$  pMpc. The redshift averaged over the spectroscopically confirmed LAEs is  $z = 6.537$ . Three out of the five spectroscopically confirmed LAEs are included in the members of the overdensity shown in Chanchaiworawit et al. (2017).

## 5.2. Implications for Cosmic Reionization

### 5.2.1. Spatial Correlation between Bright LAEs and Overdensities

To study the origin of the bright-end excess of  $\text{Ly}\alpha$  LFs at  $z = 5.7$  and  $6.6$  (Matthee et al. 2015; Santos et al. 2016; Bagley et al. 2017; Konno et al. 2018), we investigate the correlation between  $\text{Ly}\alpha$  luminosity and overdensity. The upper (lower) panel of Figure 19 shows the relation between the  $\text{Ly}\alpha$  luminosity  $L_{\text{Ly}\alpha}$  and the large-scale LAE overdensity  $\delta_{\text{LS}}$  for  $z = 5.7$  ( $6.6$ ) LAEs. Here,  $\delta_{\text{LS}}$  is defined by a circle with a radius of  $0^{\circ}20$  that corresponds to  $\sim 30$  cMpc at  $z \sim 6$ , comparable with the size of typical ionized bubbles at this

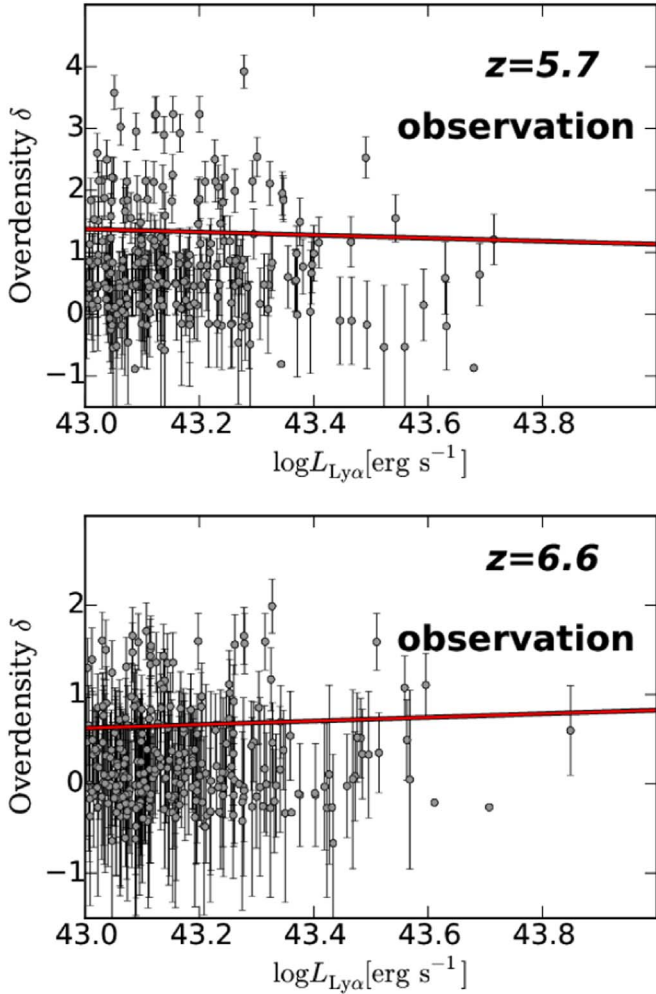


**Figure 19.**  $\text{Ly}\alpha$  luminosity  $L_{\text{Ly}\alpha}$  as a function of large-scale overdensity  $\delta_{\text{LS}}$  for the HSC LAEs (gray circles) at  $z = 5.7$  (upper panel) and  $6.6$  (lower panel), respectively. The red line indicates the best-fit linear function.

redshift predicted by Furlanetto et al. (2006; see the  $\delta$  defined with a circular radius of  $0.07$ , Section 5.1). With the results of Figure 19, we calculate a Spearman’s rank correlation coefficient  $\rho$  and a  $p$ -value to test the existence of the correlation between  $L_{\text{Ly}\alpha}$  and  $\delta_{\text{LS}}$ . We obtain  $\rho = -0.018$  ( $-0.03$ ) with  $p$ -value =  $0.78$  ( $0.60$ ) for  $z = 5.7$  ( $6.6$ ) LAEs, which suggests that there are no significant correlations between  $L_{\text{Ly}\alpha}$  and  $\delta_{\text{LS}}$ . This result indicates that bright  $L_{\text{Ly}\alpha}$  LAEs are not selectively placed at the overdensity and that there is no clear evidence connecting the bright-end LF excess and the ionized bubble. Because the statistical uncertainty of this analysis is still large, it is not a conclusive result. There is another possibility that the faint  $\text{Ly}\alpha$  sources are hard to detect due to their surrounding neutral IGM. However, there is an increasing possibility that the ionized bubbles and the bright-end LF excess may not be related. For the other possible origins of the bright-end excess, Konno et al. (2018) discussed the AGN/low- $z$  contamination and blended merging galaxies. Feedback effects from quasars should also be discussed (Kashikawa et al. 2007; Uchiyama et al. 2019). We should discuss these other possibilities more seriously.

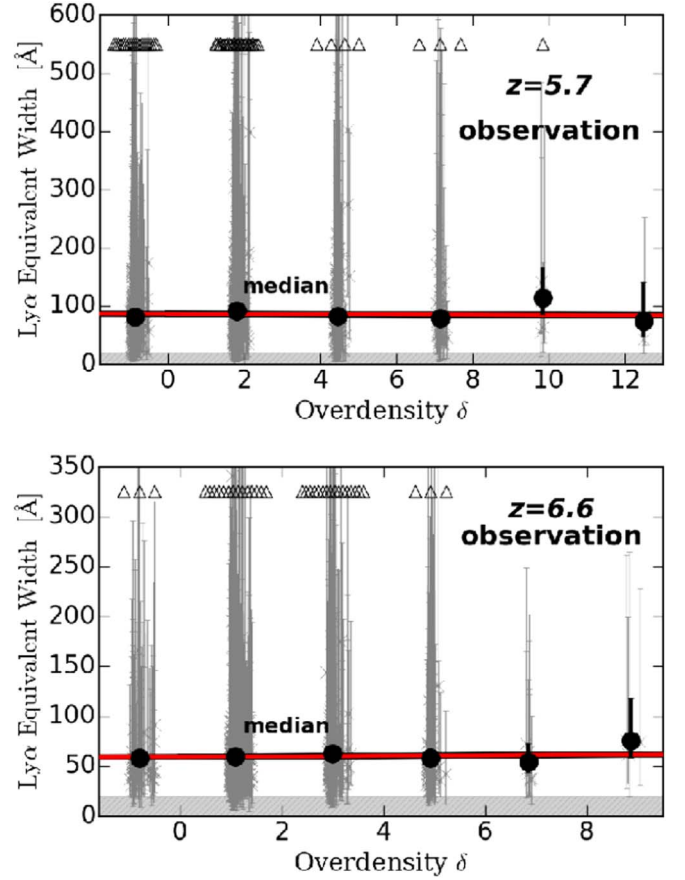


**Figure 20.**  $\text{Ly}\alpha$  EW and overdensity  $\delta$  for our HSC LAEs at  $z = 5.7$  (upper panel) and  $6.6$  (lower panel), respectively. The gray crosses with the error bars represent our HSC LAEs. The filled circles with the error bars indicate the median values of  $\text{EW}_{\text{Ly}\alpha}^{\text{rest}}$  in each subsample. The open triangles show the lower limits of our HSC LAEs with best-estimate  $\text{EW}_{\text{Ly}\alpha}^{\text{rest}}$  values exceeding  $550$  ( $325$ )  $\text{\AA}$  at  $z = 5.7$  ( $6.6$ ). For display purposes, the unfilled triangles are slightly shifted toward the abscissa axis direction. The red line represents the best-fit linear function. The gray region indicates the  $\text{Ly}\alpha$  EW selection limit.

### 5.2.2. Correlation between $\text{Ly}\alpha$ EW and Overdensity

The upper (lower) panel of Figure 20 presents  $\text{EW}_{\text{Ly}\alpha}^{\text{rest}}$  as a function of  $\delta$  for our HSC LAEs at  $z = 5.7$  ( $6.6$ ). We calculate  $\delta$  at the position centered at an LAE in the same manner as Section 5.1. We make subsamples of our LAEs divided by  $\delta$ . For the  $\text{EW}_{\text{Ly}\alpha}^{\text{rest}}$  estimates in Figure 20, we need careful calculations. This is because none of the LAE continua (used for the  $\text{EW}_{\text{Ly}\alpha}^{\text{rest}}$  estimates) are detected in our broadband data. We generate 100,000 data sets for each subsample, randomly changing  $\text{NB816}$  ( $\text{NB921}$ ) and  $z$ - ( $y$ -) band magnitudes following the Gaussian distribution with mean and sigma defined as the observational measurement and error magnitudes, respectively. We calculate  $\text{EW}_{\text{Ly}\alpha}^{\text{rest}}$  in the same manner as Shibuya et al. (2018a) for each data set. In each subsample, the  $\text{EW}_{\text{Ly}\alpha}^{\text{rest}}$  value and  $1\sigma$  upper (lower) error are obtained as the 50th and 84th (16th) percentile of the distribution, respectively. These  $\text{EW}_{\text{Ly}\alpha}^{\text{rest}}$  values and  $1\sigma$  upper (lower) errors are shown in Figure 20. In Figure 20, we perform chi-square fitting of the linear function to the  $\text{EW}_{\text{Ly}\alpha}^{\text{rest}}-\delta$  relations, and obtain the best-fit parameters,  $\alpha$  and  $\text{EW}_{\delta=0}$ , defined in Section 4. Because the theoretical model predicts that the value of  $\alpha$  increases from  $z = 5.7$  to  $6.6$  (Section 4), we show the redshift evolution of the  $\alpha$  of the observational results in Figure 21. Figure 21

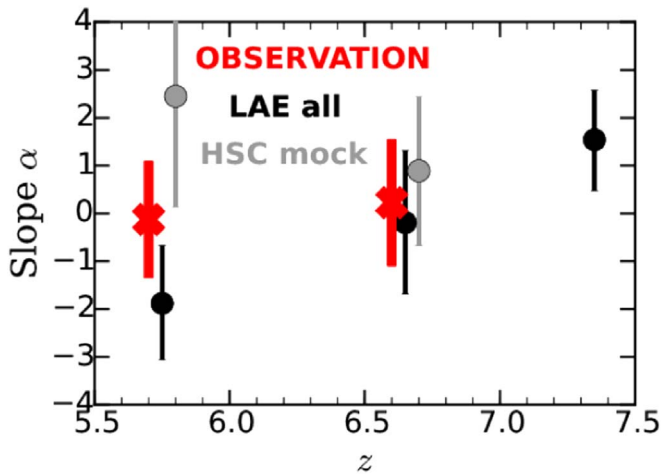


**Figure 21.** Redshift evolution of the slope  $\alpha$ . The red crosses denote the HSC LAEs, while the gray (black) circles show the model predictions with the samples of “HSC mock” and “LAE all,” respectively. To avoid overlaps of the symbols, we slightly shift the black and gray circles by 0.05 and 0.10 in redshift, respectively.

indicates that there is no significant evolution of the  $EW_{Ly\alpha}^{\text{rest}}-\delta$  relation from  $z = 5.7$  to  $6.6$  beyond the uncertainties accomplished with our HSC data obtained so far.

### 5.2.3. Comparison with the Theoretical Model

We compare the results of Section 5.2.2 with the theoretical model of Inoue et al. (2018). We select mock LAEs with the same magnitude and color criteria as those of our HSC LAEs. We thus obtain 815 (134) mock LAEs for  $z = 5.7$  (6.6), which are referred to as “HSC mock.” We derive the best-fit parameters and errors for HSC mock in the same way as Section 5.2.2. Note that we also apply the selection limits of the  $Ly\alpha$  EW, which are similar to those of the HSC LAE samples. Figure 21 presents the redshift evolution of the slope  $\alpha$  of “HSC mock” at  $z = 5.7$  and  $6.6$ . (In this model, the average neutral hydrogen fraction in the IGM at  $z = 5.7$  and  $6.6$  are  $\log x_{\text{HI}} = -3.9$  and  $-0.36$ , respectively.) The model does not show significant evolution of the  $EW_{Ly\alpha}^{\text{rest}}-\delta$  relation beyond the statistical errors, which is consistent with that of the HSC LAE samples. The model suggests that the present HSC LAE samples are not large enough to test the existence of the ionized bubbles and the inside-out scenario of cosmic reionization. The HSC survey is underway, which will significantly enlarge the sample with the wider and deeper data for LAEs at  $z = 5.7$  and  $6.6$ , and make a new sample of LAEs at  $z = 7.3$ . There is a possibility that the evolution of the  $EW_{Ly\alpha}^{\text{rest}}-\delta$  relation from  $z = 5.7$  to  $7.3$  may be identified by upcoming HSC observations providing large samples of LAEs at  $z = 5.7-7.3$ . The ionized bubbles and the inside-out scenario should be tested in forthcoming studies with large samples of LAEs at  $z = 5.7-7.3$ .

## 6. Summary

Here, we study LAE overdensities at  $z = 5.7$  and  $6.6$  with the early data sets of the HSC-SSP survey based on the 2230 LAEs obtained in the SILVERRUSH program. We identify the LAE overdensities and discuss cosmic reionization with the properties of LAEs: overdensity  $\delta$ ,  $Ly\alpha$  luminosity  $L_{Ly\alpha}$ , and











the rest-frame  $Ly\alpha$  equivalent width  $EW_{Ly\alpha}^{\text{rest}}$ . Our major results are listed below:

1. We calculate the LAE overdensity  $\delta$  with the samples of the HSC LAEs at  $z = 5.7$  and  $6.6$ . We identify 14 (26)  $z = 5.7$  (6.6) LAE overdensities, six of which have one to 13 spectroscopically confirmed LAEs. We conduct Monte Carlo simulations to estimate how many LAE overdensities are found by chance for randomly distributed sources. By subtracting the expected number of overdensities found by chance, the effective number of LAE overdensities at  $z = 5.7$  (6.6) is estimated to be six (five). We compare the LAE overdensities with the cosmological  $Ly\alpha$  RT models, and find that more than half of these LAE overdensities (60% and 58% of the LAE overdensities at  $z = 5.7$  and  $6.6$ ) are progenitors of the present-day clusters with mass of  $\gtrsim 10^{14} M_{\odot}$ . These 14 (26) LAE overdensities are thus protocluster candidates at  $z = 5.7$  (6.6), which are listed in Table 4.
2. We investigate the correlation between  $L_{Ly\alpha}$  and  $\delta$  with the HSC LAEs. We obtain a Spearman’s rank correlation coefficient  $\rho = -0.018$  (0.03) with  $p$ -value = 0.78 (0.60) for  $z = 5.7$  (6.6) LAEs, which indicates that there is no evidence of significant correlations between  $L_{Ly\alpha}$  and  $\delta$  beyond the observational uncertainties. Our result is related to the recent discussion on the bright-end excess of  $Ly\alpha$  LFs at  $z = 5.7$  and  $6.6$  as found in Konno et al. (2018). Regarding the physical reason for the bright-end excess, it has been suggested that bright galaxies selectively existing in an overdensity region are near the center of ionized bubbles that allow  $Ly\alpha$  photons to escape from the partly neutral IGM at the EoR. Because our results show no correlation between  $L_{Ly\alpha}$  and  $\delta$ , there is no evidence supporting this idea.
3. We study the relations between  $EW_{Ly\alpha}^{\text{rest}}$  and  $\delta$  at  $z = 5.7$  and  $6.6$ . We fit a linear function to the  $EW_{Ly\alpha}^{\text{rest}}-\delta$  data, and find that the slope (the relation) does not evolve (does not steepen) from  $z = 5.7$  to  $6.6$  beyond the errors. The cosmological reionization model with the  $Ly\alpha$  RT suggests that the slope steepens toward the early EoR with a high neutral hydrogen fraction in the inside-out reionization scenario, because the ionized bubbles around galaxy overdensities make the escape of  $Ly\alpha$  emission from the partly neutral IGM at the EoR easier. Although the model suggests that the statistical accuracy of our HSC data is not high enough to investigate this steepening, so far we find no such steepening in the available HSC data. This study has a role in showing a forecast of future works after the data release of scheduled HSC narrowband observations. The model suggests that there is a possibility of detecting the evolution of the  $EW_{Ly\alpha}^{\text{rest}}-\delta$  relation from  $z = 5.7$  to  $7.3$  with the scheduled HSC narrowband observations that will make larger samples of LAEs at  $z = 5.7-6.6$  as well as a new sample of LAEs at  $z = 7.3$ .

We are grateful to Richard S. Ellis, Ryohei Itoh, Shotaro Kikuchihara, Haruka Kusakabe, Hilmi Miftahul, Shiro Mukae, Yuma Sugahara, Hidenobu Yajima, Haibin Zhang, and Zheng Zheng for useful comments and discussions. We thank Shingo Shinogi for providing information about the Keck/DEIMOS spectra of  $z = 5.7$  LAEs. We also thank Janice Lee and Ivelina Momcheva for providing Magellan/IMACS spectra of  $z = 5.7$

LAEs that were taken as mask fillers. The Hyper Suprime-Cam (HSC) collaboration includes the astronomical communities of Japan and Taiwan, and Princeton University. The HSC instrumentation and software were developed by the National Astronomical Observatory of Japan (NAOJ), the Kavli Institute for the Physics and Mathematics of the Universe (Kavli IPMU), the University of Tokyo, the High Energy Accelerator Research Organization (KEK), the Academia Sinica Institute for Astronomy and Astrophysics in Taiwan (ASIAA), and Princeton University. Funding was contributed by the FIRST program from the Japanese Cabinet Office, the Ministry of Education, Culture, Sports, Science and Technology (MEXT), the Japan Society for the Promotion of Science (JSPS), Japan Science and Technology Agency (JST), the Toray Science Foundation, NAOJ, Kavli IPMU, KEK, ASIAA, and Princeton University. The Pan-STARRS1 Surveys (PS1) have been made possible through contributions of the Institute for Astronomy, the University of Hawaii, the Pan-STARRS Project Office, the Max-Planck Society and its participating institutes, the Max Planck Institute for Astronomy, Heidelberg and the Max Planck Institute for Extraterrestrial Physics, Garching, The Johns Hopkins University, Durham University, the University of Edinburgh, Queen's University Belfast, the Harvard-Smithsonian Center for Astrophysics, the Las Cumbres Observatory Global Telescope Network Incorporated, the National Central University of Taiwan, the Space Telescope Science Institute, the National Aeronautics and Space Administration under grant No. NNX08AR22G issued through the Planetary Science Division of the NASA Science Mission Directorate, the National Science Foundation under grant No. AST-1238877, the University of Maryland, and Eötvös Loránd University (ELTE). This paper makes use of software developed for the Large Synoptic Survey Telescope. We thank the LSST Project for making their code available as free software at <http://dm.lsst.org>. Based in part on data collected at the Subaru Telescope and retrieved from the HSC data archive system, which is operated by the Subaru Telescope and Astronomy Data Center at National Astronomical Observatory of Japan. The NB816 filter was supported by Ehime University (PI: Y. Taniguchi). The NB921 filter was supported by KAKENHI (23244025) Grant-in-Aid for Scientific Research (A) through the Japan Society for the Promotion of Science (PI: M. Ouchi). This work is supported by World Premier International Research Center Initiative (WPI Initiative), MEXT, Japan, and KAKENHI (15H02064) Grant-in-Aid for Scientific Research (A) through the Japan Society for the Promotion of Science. This research was supported by a grant from the Hayakawa Satio Fund awarded by the Astronomical Society of Japan.

### ORCID iDs

Masami Ouchi  <https://orcid.org/0000-0002-1049-6658>  
 Jun Toshikawa  <https://orcid.org/0000-0001-5394-242X>  
 Yuichi Harikane  <https://orcid.org/0000-0002-6047-430X>  
 Takashi Kojima  <https://orcid.org/0000-0001-5780-1886>  
 Yi-Kuan Chiang  <https://orcid.org/0000-0001-6320-261X>  
 Nobunari Kashikawa  <https://orcid.org/0000-0001-5493-6259>  
 Roderik Overzier  <https://orcid.org/0000-0002-8214-7617>  
 Akio K. Inoue  <https://orcid.org/0000-0002-7779-8677>  
 Seiji Fujimoto  <https://orcid.org/0000-0001-7201-5066>  
 Shogo Ishikawa  <https://orcid.org/0000-0002-2118-4211>

Kei Ito  <https://orcid.org/0000-0002-9453-0381>

Masayuki Tanaka  <https://orcid.org/0000-0002-5011-5178>

### References

- Aihara, H., Arimoto, N., Armstrong, R., et al. 2018a, *PASJ*, **70**, S4  
 Aihara, H., Armstrong, R., Bickerton, S., et al. 2018b, *PASJ*, **70**, S8  
 Axelrod, T., Kantor, J., Lupton, R. H., & Pierfederici, F. 2010, *Proc. SPIE*, **7740**, 774015  
 Bagley, M. B., Scarlata, C., Henry, A., et al. 2017, *ApJ*, **837**, 11  
 Becker, G. D., Bolton, J. S., Madau, P., et al. 2015, *MNRAS*, **447**, 3402  
 Bertin, E., & Arnouts, S. 1996, *A&AS*, **117**, 393  
 Bolton, J. S., Haehnelt, M. G., Warren, S. J., et al. 2011, *MNRAS*, **416**, L70  
 Bosch, J., Armstrong, R., Bickerton, S., et al. 2018, *PASJ*, **70**, S5  
 Bosman, S. E. I., Fan, X., Jiang, L., et al. 2018, *MNRAS*, **479**, 1055  
 Bouwens, R. J., Illingworth, G. D., Oesch, P. A., et al. 2015, *ApJ*, **811**, 140  
 Chanchaiworawit, K., Guzman, R., Rodriguez Espinosa, J.M., et al. 2017, *MNRAS*, **469**, 2646  
 Chiang, Y.-K., Overzier, R., & Gebhardt, K. 2013, *ApJ*, **779**, 127  
 Chiang, Y.-K., Overzier, R. A., Gebhardt, K., & Henriques, B. 2017, *ApJL*, **844**, L23  
 Chornock, R., Berger, E., Fox, D. B., et al. 2013, *ApJ*, **774**, 26  
 Darvish, B., Mobasher, B., Sobral, D., Scoville, N., & Aragon-Calvo, M. 2015, *ApJ*, **805**, 121  
 Davis, M., Faber, S.M., Newman, J., et al. 2003, *Proc. SPIE*, **4834**, 161  
 Dijkstra, M., Gronke, M., & Venkatesan, A. 2016, *ApJ*, **828**, 71  
 Dijkstra, M., Mesinger, A., & Wyithe, J. S. B. 2011, *MNRAS*, **414**, 2139  
 Drake, A. B., Guiderdoni, B., Blaizot, J., et al. 2017, *MNRAS*, **471**, 267  
 Dressler, A., Hare, T., Bigelow, B. C., & Osip, D. J. 2006, *Proc. SPIE*, **6269**, 62690F  
 Faber, S. M., Phillips, A.C., Kibrick, R.I., et al. 2003, *Proc. SPIE*, **4841**, 1657  
 Fan, X., Strauss, M.A., Becker, R.H., et al. 2006, *AJ*, **132**, 117  
 Finlator, K., Özel, F., Davé, R., & Oppenheimer, B. D. 2009, *MNRAS*, **400**, 1049  
 Franck, J. R., & McGaugh, S. S. 2016a, *ApJ*, **833**, 15  
 Franck, J. R., & McGaugh, S. S. 2016b, *ApJ*, **817**, 158  
 Furlanetto, S. R., Zaldarriaga, M., & Hernquist, L. 2006, *MNRAS*, **365**, 1012  
 Furusawa, H., Koike, M., Takata, T., et al. 2018, *PASJ*, **70**, S3psx079  
 Gehrels, N. 1986, *ApJ*, **303**, 336  
 Goto, T., Utsumi, Y., Hattori, T., Miyazaki, S., & Yamauchi, C. 2011, *MNRAS*, **415**, L1  
 Guzmán, R., Chanchaiworawit, K., Rodriguez-Espinosa, J.M., et al. 2017, in *Early Stages of Galaxy Cluster Formation 12*  
 Hamana, T., Yamada, T., Ouchi, M., Iwata, I., & Kodama, T. 2006, *MNRAS*, **369**, 1929  
 Harikane, Y., Ouchi, M., Shibuya, T., et al. 2018, *ApJ*, **859**, 84  
 Harikane, Y., Ouchi, M., Ono, Y., et al. 2018, *PASJ*, **70**, S11  
 Higuchi, R., et al. 2019, in *IAU Symp. 341, PanModel2018 Challenges in Panchromatic Galaxy Modelling with Next Generation Facilities* in press  
 Hu, E. M., Cowie, L. L., Songaila, A., et al. 2016, *ApJL*, **825**, L7  
 Iliev, I. T., Mellema, G., Pen, U.-L., et al. 2006, *MNRAS*, **369**, 1625  
 Inoue, A. K., Hasegawa, K., Ishiyama, T., et al. 2018, *PASJ*, **70**, 55  
 Ishigaki, M., Kawamata, R., Ouchi, M., Oguri, M., & Shimasaku, K. 2017, *arXiv:1702.04867*  
 Ishigaki, M., Ouchi, M., & Harikane, Y. 2016, *ApJ*, **822**, 5  
 Ivezic, Z., Kahn, S.M., Tyson, J.A., et al. 2019, *ApJ*, **873**, 111  
 Iye, M., Karoji, H., Ando, H., et al. 2004, *PASJ*, **56**, 381  
 Jensen, H., Hayes, M., Iliev, I. T., et al. 2014, *MNRAS*, **444**, 2114  
 Jiang, L., Shen, Y., Bian, F., et al. 2017, *ApJ*, **846**, 134  
 Jiang, L., Wu, J., Bian, F., et al. 2018, *NatAs*, **2**, 962  
 Jurić, M., Kantor, J., Lim, K.T., et al. 2015, in *Astronomical Data Analysis Software and Systems XXV*, ed. N.P.F. Lorente, K. Shorridge, & R. Wayth (San Francisco, CA: ASP), 279  
 Kakiichi, K., Dijkstra, M., Ciardi, B., & Graziani, L. 2016, *MNRAS*, **463**, 4019  
 Kashikawa, N., Kitayama, T., Doi, M., et al. 2007, *ApJ*, **663**, 765  
 Kashikawa, N., Shimasaku, K., Malkan, M., et al. 2006, *ApJ*, **648**, 7  
 Kashikawa, N., Shimasaku, K., Matsuda, Y., et al. 2011, *ApJ*, **734**, 119  
 Komiyama, Y., Obuchi, Y., Nakaya, H., et al. 2018, *PASJ*, **70**, S2  
 Konno, A., Ouchi, M., Ono, Y., et al. 2014, *ApJ*, **797**, 16  
 Konno, A., Ouchi, M., Shibuya, T., et al. 2018, *PASJ*, **70**, S16  
 Lee, J. C., Ly, C., Spitzer, L., et al. 2012, *PASP*, **124**, 782  
 Lovell, C. C., Thomas, P. A., & Wilkins, S. M. 2018, *MNRAS*, **474**, 4612  
 Magnier, E. A., Schaffly, E., Finkbeiner, D., et al. 2013, *ApJS*, **205**, 20  
 Malhotra, S., & Rhoads, J. E. 2004, *ApJL*, **617**, L5  
 Mallery, R. P., Mobasher, B., Capak, P., et al. 2012, *ApJ*, **760**, 128  
 Matthee, J., Sobral, D., Gronke, M., et al. 2018, *A&A*, **619**, A136

- Matthee, J., Sobral, D., Santos, S., et al. 2015, *MNRAS*, 451, 400
- McGreer, I. D., Mesinger, A., & D’Odorico, V. 2015, *MNRAS*, 447, 499
- McQuinn, M. 2012, *MNRAS*, 426, 1349
- Mesinger, A., Ferrara, A., & Spiegel, D. S. 2013, *MNRAS*, 431, 621
- Miralda-Escudé, J., Haehnelt, M., & Rees, M. J. 2000, *ApJ*, 530, 1
- Miyazaki, S., Komiyama, Y., Sekiguchi, M., et al. 2002, *PASJ*, 54, 833
- Miyazaki, S., Komiyama, Y., Kawanomoto, S., et al. 2018, *PASJ*, 70, S1
- Momcheva, I. G., Lee, J. C., Ly, C., et al. 2013, *AJ*, 145, 47
- Nakamoto, T., Umemura, M., & Susa, H. 2001, *MNRAS*, 321, 593
- Ono, Y., Ouchi, M., Mobasher, B., et al. 2012, *ApJ*, 744, 83
- Ono, Y., Ouchi, M., Harikane, Y., et al. 2018, *PASJ*, 70, S10
- Ota, K., Iye, M., Kashikawa, N., et al. 2010, *ApJ*, 722, 803
- Ouchi, M., Shimasaku, K., Akiyama, M., et al. 2005, *ApJL*, 620, L1
- Ouchi, M., Shimasaku, K., Akiyama, M., et al. 2008, *ApJS*, 176, 301
- Ouchi, M., Ono, Y., Egami, E., et al. 2009, *ApJ*, 696, 1164
- Ouchi, M., Shimasaku, K., Furusawa, H., et al. 2010, *ApJ*, 723, 869
- Ouchi, M., Harikane, Y., Shibuya, T., et al. 2018, *PASJ*, 70, S13
- Overzier, R. A. 2016, *A&ARv*, 24, 14
- Planck Collaboration et al. 2016, *A&A*, 596, A108
- Reiprich, T. H., & Böhringer, H. 2002, *ApJ*, 567, 716
- Robertson, B. E., Ellis, R. S., Furlanetto, S. R., & Dunlop, J. S. 2015, *ApJL*, 802, L19
- Santos, S., Sobral, D., & Matthee, J. 2016, *MNRAS*, 463, 1678
- Schlafly, E. F., Finkbeiner, D.P., Juri, C.M., et al. 2012, *ApJ*, 756, 158
- Shibuya, T., Ouchi, M., Nakajima, K., et al. 2014, *ApJ*, 788, 74
- Shibuya, T., Ouchi, M., Konno, A., et al. 2018a, *PASJ*, 70, S14
- Shibuya, T., Ouchi, M., Harikane, Y., et al. 2018b, *PASJ*, 70, S15
- Sobral, D., Matthee, J., Darvish, B., et al. 2015, *ApJ*, 808, 139
- Sobral, D., Santos, S., Matthee, J., et al. 2018, *MNRAS*, 476, 4725
- Stark, D. P., Ellis, R. S., & Ouchi, M. 2011, *ApJL*, 728, L2
- Tonry, J. L., Stubbs, C.W., Lykke, K.R., et al. 2012, *ApJ*, 750, 99
- Toshikawa, J., Kashikawa, N., Ota, K., et al. 2012, *ApJ*, 750, 137
- Toshikawa, J., Kashikawa, N., Overzier, R., et al. 2014, *ApJ*, 792, 15
- Toshikawa, J., Uchiyama, H., Kashikawa, N., et al. 2018, *PASJ*, 70, S12
- Uchiyama, H., Kashikawa, N., Overzier, R., et al. 2019, *ApJ*, 870, 45
- Utsumi, Y., Goto, T., Kashikawa, N., et al. 2010, *ApJ*, 721, 1680